Modeling interactions of natural and twophase fluid-filled fracture propagation in porous media

Sanghyun Lee & Mary F. Wheeler

Computational Geosciences

Modeling, Simulation and Data Analysis

ISSN 1420-0597

Comput Geosci DOI 10.1007/s10596-020-09975-0





Your article is protected by copyright and all rights are held exclusively by Springer Nature Switzerland AG. This e-offprint is for personal use only and shall not be selfarchived in electronic repositories. If you wish to self-archive your article, please use the accepted manuscript version for posting on your own website. You may further deposit the accepted manuscript version in any repository, provided it is only made publicly available 12 months after official publication or later and provided acknowledgement is given to the original source of publication and a link is inserted to the published article on Springer's website. The link must be accompanied by the following text: "The final publication is available at link.springer.com".



Computational Geosciences https://doi.org/10.1007/s10596-020-09975-0

ORIGINAL PAPER



Modeling interactions of natural and two-phase fluid-filled fracture propagation in porous media

Sanghyun Lee¹ • Mary F. Wheeler²

Received: 7 June 2019 / Accepted: 11 May 2020 © Springer Nature Switzerland AG 2020

Abstract

In this paper, a novel computational framework is introduced for simulation of multiphase flow, geomechanics, and fracture propagation in porous media based on Biot's model for poroelasticity by focusing on interactions between hydraulic and natural fractures. Since realistic porous media contain many natural fractures, it is important not only to stimulate hydraulic fractures but also to study the interaction between natural and hydraulic fractures. Here, state-of-the-art numerical modeling of natural and hydraulic fractures using a diffusive adaptive finite element phase field approach is employed. The locally mass conservative enriched Galerkin finite element methods (EG) are utilized to model two-phase flow in propagating fractures with relative permeability and capillary pressure. Geomechanics approximated by a continuous Galerkin finite element method is coupled to multiphase flow by applying an iteratively coupled scheme. Numerical examples are presented that demonstrate the effectiveness of this framework for different propagation scenarios by varying the degrees of physics. In addition, the capabilities to perform high-fidelity simulations on complex fracture networks, with randomly joined diffusive natural fractures, are illustrated.

Keywords Phase field fracture · Natural fracture network · Multiphase flow · Fracture propagation

1 Introduction

Hydrocarbon production from unconventional reservoirs has become an integral source of energy for the USA. Almost 50% of total US crude oil and gas production is from shale and tight reservoirs; this percentage will increase in the years to come [90]. Most of the hydrocarbons recovered in unconventional reservoirs come from the fractures due to the very low permeability. Recent studies [35, 52] reveal that unconventional reservoirs contain complex natural fracture networks. Thus, in stimulating hydraulic fractures, it is important to study the interactions between natural fractures

⊠ Sanghyun Lee lee@math.fsu.edu

Mary F. Wheeler mfw@ices.utexas.edu

Published online: 18 July 2020

- Department of Mathematics, Florida State University, 208 Love Building 1017 Academic Way, Tallahassee, FL 32306, USA
- The Center for Subsurface Modeling, The University of Texas at Austin, 201 East 24th Street, Austin, TX 78712, USA

and hydraulic fractures especially in optimizing fracture treatments [30]. This has been substantiated in existing experimental and field studies [79, 91]; namely, the intersections between natural and hydraulic fractures can effect the fracture propagation path, fluid flow, fracture width, and transport of the proppant. For example, see Fig. 1. Moreover, recent field observations have shown through extended field studies [44] that current stimulation models fall short in predicting hydraulic fracture geometries, proppant placement and transport, flowback, the effects of stress shadowing development, and perhaps more importantly is treating parent/children fracture patterns. Hence, there is a research need for better explaining, predicting, and modeling realistic stimulation processes.

Simulation of flow in a fractured porous media can be treated as modeling network flow. A reference fracture network (RFN) obtained from field data is required in order to undertake integrated research efforts, which range from characterization of the RFN to reservoir production to restimulation. We now briefly describe some of the modeling approaches that have been applied.

Conventional hydraulically fractured systems have assumed symmetric, planar, bi-wing crack geometries. This has led to classical fracturing models such as PKN [80] and



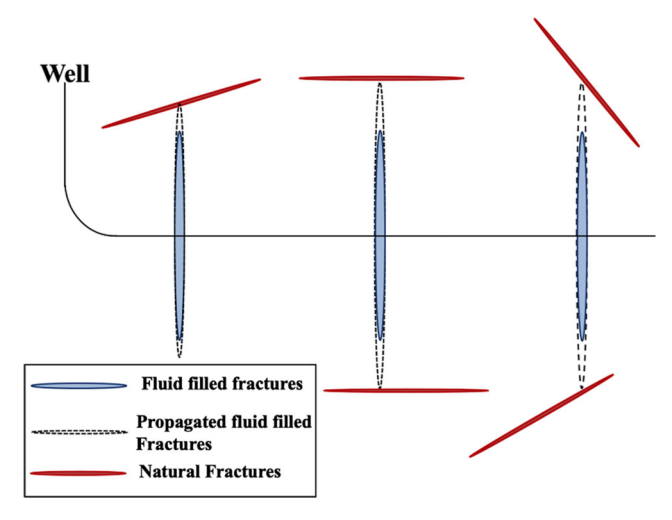
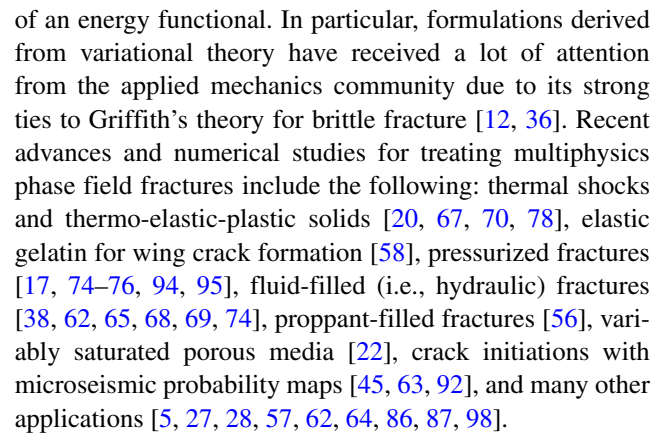


Fig. 1 Interactions between natural and hydraulic fractures

KGD [99], and the current planar 3D (PL3D) models. One of the most popular models, the discrete fracture network model (DFN) computes fluid flow and deformation in a discrete fracture network. The model has the ability to represent propagation through an additional set of predetermined paths, representing plausible degrees of liberty. In other words, instead of placing a fracture plane, calculating a tip stress, and then determining the orientation and next plane placement, all planes are placed and, depending on orientations and net pressures, they are activated (opened). Before identifying the locations of any of the fractures, a population of lengths and orientations is chosen according to characterization analysis (statistical distributions). The definition of a numerical reservoir representation, either leading to a classical dual-media approach or using an un-structured mesh (DDFN), including a matrix proximity function (MInC type matrix refinement) accounting for transient effects From the theoretical point of view, this approach can be considered as a UEDFM method (Unstructured Embedded Discrete Fracture Model). An incomplete list of references includes [24, 31, 42, 48, 53, 66, 89, 97, 100, 100]. We remark that limited results have been obtained for conventional and DFN schemes coupling geomechanics and proppant transport for re-fracturing.

In this paper, we focus on a phase field approach for fracture propagation in a poroelastic medium based on Biot's model. The phase field methodology has become a powerful tool for modeling the evolution of microstructures and their interactions of defects in a wide range of materials and physics. The accurate simulation of fracture evolution in solids is a major challenge for computational algorithms, in large part due to crack paths that are generally unknown a priori. In this regard, phase field approaches have shown great potential with their ability to automatically determine the direction of crack propagation through minimization



One strength of phase field modeling lies in the fact that there are no additional constitutive rules or criteria required within the theory that dictate when a crack should nucleate, grow, change direction, or split into multiple cracks. Also, the interactions between fluid filled (i.e., hydraulic) and natural fractures and their growth emerge as solutions to the system of governing partial differential equations, Biot's poroelasticity model [14, 15]. Thus, computing additional stress intensity factors near the fracture tips is intrinsically embedded in the model [47]. In addition, all computations are performed entirely on the initial, un-deformed configuration. Thus, there is no need to disconnect, eliminate, or move elements or introduce additional discontinuous basis functions, as is commonly done in the discrete crack computational fracture mechanics approaches. This results in a significant simplification of the numerical implementation to handle realistic heterogeneous properties of porous media with dynamic mesh adaptivity, and a simple and direct pathway from two-dimensional to three-dimensional applications. Moreover, since our phase field model is based on a continuum approach and Biot's model, coupling other multiphysics phenomena and extension to different applications such as proppant transport and nonlinear mechanics (plasticity) are possible [55, 56, 58, 63, 85].

Here, we focus on interactions between natural fractures and hydraulic fractures in porous media. In particular, the natural fractures are described by utilizing the diffusive approach and hydraulic fractures propagate with the injection of two-phase flow [55]. Our objective is to demonstrate the effects of pressure coupled geomechanics in fracture networks. This work however is incomplete in addressing realistic field and laboratory issues. For example, there is little understanding and virtually no published complete data yet on intersection of hydraulic fractures with natural fractures. In summary, we point out that the novelties of phase field modeling that we are addressing in this paper are the following:

 Presents joining and branching fractures between hydraulic and natural fractures by employing the phase field approach with two-phase flow,



- Demonstrates the pressure drops which could be utilized as the indication of the joining,
- Considers the flowback processes by applying the current developed model.

The paper is divided into five additional sections. In Section 2, we describe phase field as a diffusive zone representation of fractures. Coupling of flow (single and multiphase) with phase field fractures is discussed in Section 3. Numerical algorithms and discretizations employed are presented in Section 4. Numerical examples are presented in Section 5 including an example for the integration of hydraulic fracture simulations with a general two-phase flow production process in porous media. Here, the permeability field is determined by computed fracture width from the proposed algorithm. It is crucial that hydraulic fracturing simulators be integrated with the production process to tackle realistic applications. Then, conclusions are provided in Section 6.

2 Phase field approach as diffusive zone representation of fractures

2.1 Phase field approach

In this work, we consider a variational approach for brittle fractures, which originated in [18, 34] based on the Griffith's theory [12, 36] and Biot's model [74]. This approach is described by applying an indicator scalar function $\varphi \in [0, 1]$ to define fractures [17, 19, 71]. Here, φ is called the phase field function, and each value of $\varphi = 0$ and $\varphi = 1$ represents broken (fracture) and unbroken (reservoir) zones, respectively. In addition, there is a transition zone $\varphi \in (0, 1)$ with the length parameter ε . Figure 2 shows the described phase field

representation. It is important to keep the diffusive zone length ε scaled in the spatial discretization parameters (e.g., mesh size) around the fracture interface.

2.2 Diffusive zone with natural fracture network and mesh adaptivity

In this section, we briefly describe an implementation of an algorithm to transfer and integrate the fracture data as values of a phase field variable. In a computational domain, any cell-by-cell natural fracture network data $(\mathbf{X}_i, \mathrm{PF}_i)$ needs to be provided for all $i=1,\cdots,N$, where N is the number of cells. This data can be obtained from any field or attained by employing the probability map methods [63, 92]. Here, $\mathbf{X}_i \in \mathbb{R}^d$ is a vector with the coordinate of the center of the cell; thus, $\mathbf{X}_i = (x_i, y_i)$ and (x_i, y_i, z_i) for two-and three-dimensional cases, respectively. Next, the discrete fracture network data (PF) is either 0 or 1 as a discontinuous indicator function. Here, PF = 0 and PF = 1 indicate fracture cell and non-fracture cell, respectively. Figure 3(a) illustrates one example of the PF data.

Then, this discontinuous cell-by-cell data (PF) is interpolated to the corresponding continuous finite element phase field function on a given finite element space. Figure 3(b) illustrates the interpolation of the PF data (either 0 or 1) to the smooth phase field function value (φ) , which has values between 0 and 1 with the diffusive zone. The interpolated PF values become an initial phase field φ^0 . This algorithm is easily implemented in parallel computing.

Finally, we emphasize the adaptive mesh refinement feature of our algorithm in Fig. 4. To obtain smooth phase field values for a given natural fracture network and use efficient amount of the meshes for further computations, adaptive mesh refinement is employed to capture and refine only near the fracture interfaces.

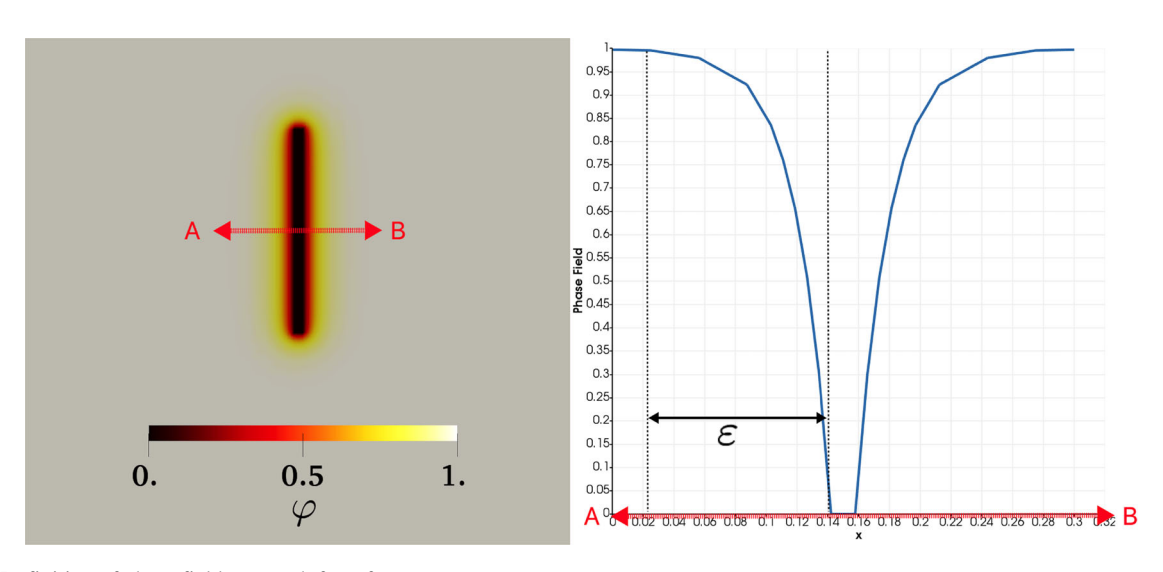
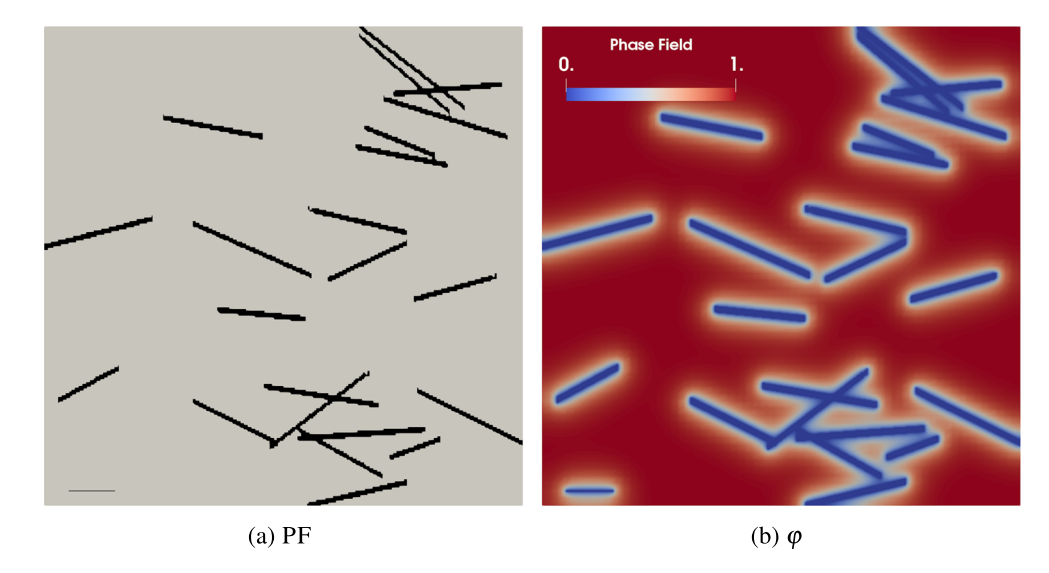


Fig. 2 Definition of phase field approach for a fracture

Fig. 3 a Discrete fracture network data (PF). b Phase field (φ) representation of **a**



3 Coupling two phase flow and mechanics with phase field fractures

We now recapitulate the essentials for the phase field modeling for pressurized and two phase flow fluid filled fractures in porous media, as described in [62, 75, 76]. Let $\mathbf{u}(\cdot, t)$: $\Lambda \times (0; T) \to \mathbb{R}^d (d \in (2,3))$ be a vector-valued displacement, $p(\cdot, t) : \Lambda \times (0; T) \to \mathbb{R}$ be a scalar-valued pressure, and $\varphi(\cdot, t): \Lambda \times (0; T) \to [0, 1]$ be a scalar-valued phase field function, where $\Lambda \in \mathbb{R}^d (d = 2, 3)$ is a computational domain with a given time [0, T] and T > 0 is the final time.

Here, $\Omega_F(t)$ is an open and connected set corresponding to the fracture and $\Omega_R(t)$ is an open and connected set corresponding to the non-fractured porous media(reservoir) material, for every $t \in [0, T]$. Thus, the entire domain is $\Lambda = \Omega_F \cup \Omega_R \cup \Gamma_F$, where $\Gamma_F = \overline{\Omega}_F \cap \overline{\Omega}_R$ is the fracture boundary. Later, the phase field, a smoothed indicator function, will be employed to redefine $\Omega_R(t)$, $\Omega_F(t)$, and $\Gamma_F(t)$. The boundary of the domain $\partial \Lambda$ splits into a Dirichlet part $\partial_D \Lambda$ and a Neumann part $\partial_N \Lambda$.

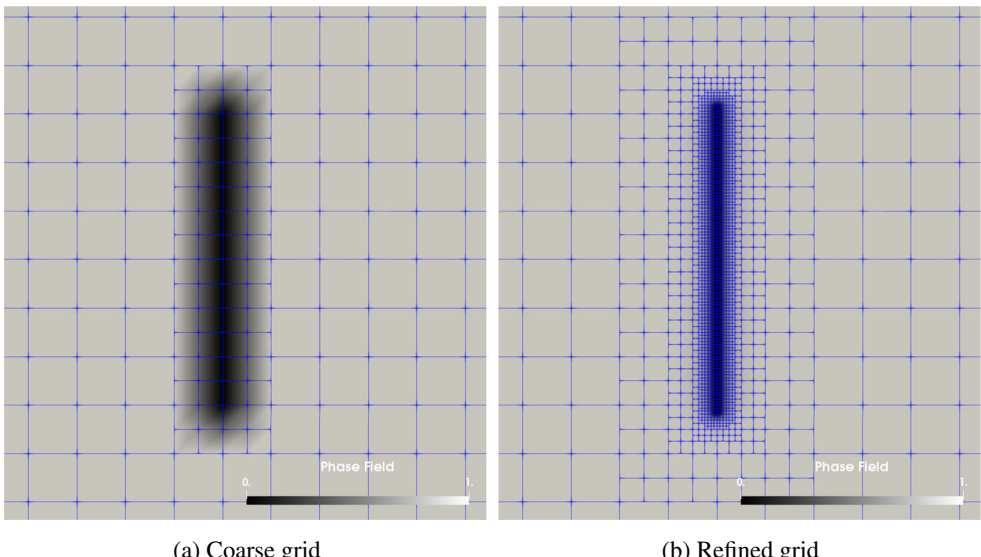
3.1 Coupling poromechanics with phase field fractures based on Biot's model

The solid displacements and the pressure in a non-fractured porous medium (reservoir) are modeled in Ω_R by the classical quasi-static elliptic-parabolic Biot's system [14, 15] for a porous solid saturated with a slightly compressible viscous fluid. Let $p_R = p|_{\Omega_R}$ be the pressure in the reservoir, then the constitutive equation for the Cauchy stress tensor is given as:

$$\sigma^{por}(\mathbf{u}, p_R) - \sigma_R^0 = \sigma_R(\mathbf{u}) - \alpha(p_R - p_R^0)I$$

in $\Omega_R \times (0, T)$, (1)

Fig. 4 Coarse and refined grids from the discrete fracture data in Fig. 3a to the smooth phase field in Fig. 3b. Meshes are only refined near the fracture interfaces



(a) Coarse grid

(b) Refined grid



where p_R^0 is the initial reservoir pressure, I is the identity tensor, σ_R^0 is the initial stress value, and $\alpha \in [0, 1]$ is the Biot's coefficient. The effective linear elastic stress tensor is:

$$\sigma_R := \sigma|_{\Omega_R} = \sigma_R(\mathbf{u}) := \lambda(\nabla \cdot \mathbf{u})I + 2G\mathbf{e}(\mathbf{u}), \tag{2}$$

where λ , G > 0 are the Lamé coefficients. The linear elastic strain tensor is given as $\mathbf{e}(\mathbf{u}) := \frac{1}{2}(\nabla \mathbf{u} + \nabla \mathbf{u}^T)$. Then, the balance of linear momentum in the solid reads:

$$-\nabla \cdot \sigma^{por}(\mathbf{u}, p_R) = \rho_s \mathbf{g} \quad \text{in } \Omega_R \times (0, T), \tag{3}$$

where ρ_s is the density of the reservoir solid and **g** is the gravity. For the simplicity in this paper, we neglect the gravity effects, and we assume homogeneous Dirichlet boundary conditions on $\partial \Lambda$ for the displacement **u**.

In fracture mechanics, Griffith's theory [12, 36] states that a fracture propagates when the strain energy release rate reaches its critical values G_c . The energy functional considering poroelasticity and Biot's model based on [18, 19, 71, 74, 76] is defined as:

$$E(\mathbf{u}, p) = \underbrace{\frac{1}{2} \int_{\Omega_R} \sigma_R(\mathbf{u}) : \mathbf{e}(\mathbf{u}) d\mathbf{x} - \int_{\Omega_R} \alpha(p_R - p_R^0) \nabla \cdot \mathbf{u} d\mathbf{x}}_{\text{Poroelastic energy}} - \underbrace{\int_{\partial \Lambda_N \cup \Gamma_F} \tau \cdot \mathbf{u} d\mathbf{s} + \underbrace{G_c \mathcal{H}^{d-1}}_{\text{Fracture energy}}}_{\text{Surface energy}}, \tag{4}$$

where τ is the traction force and \mathcal{H}^{d-1} is the Hausdorff measure (length (d=2) or surface (d=3) of a fracture).

The main idea for the phase field formulation utilizes the elliptic (Ambrosio-Tortorelli) functional [7, 8]. The phase field is coupled with the above energy functional through the Ambrosio-Tortorelli elliptic functionals by replacing the Hausdorff measure of the fracture energy in a computable form as:

$$E(\mathbf{u}, p, \varphi) = \frac{1}{2} \int_{\Lambda} \varphi^{2} \sigma_{R}(\mathbf{u}) : \mathbf{e}(\mathbf{u}) d\mathbf{x}$$

$$- \int_{\Lambda} \varphi^{2} \alpha (p_{R} - p_{R}^{0}) \nabla \cdot \mathbf{u} d\mathbf{x}$$

$$- \int_{\partial \Lambda_{N} \cup \Gamma_{F}} \tau \cdot \mathbf{u} d\mathbf{s}$$

$$+ G_{c} \int_{\Lambda} \left(\frac{1}{2\varepsilon} (1 - \varphi)^{2} + \frac{\varepsilon}{2} (\nabla \varphi)^{2} \right) d\mathbf{x}. \quad (5)$$

We note that Eq. 5 is rewritten from Eq. 4 by also extending the poroelastic energy defined in Ω_R to the global domain Λ . This is accomplished by multiplying the phase

field function φ^2 for the entire domain: the terms in the energy functional E. Thus, the poroelastic energy vanishes when $\varphi=0$, and $\varphi=0$ indicates a fracture domain. On the other hand, the fracture energy multiplied by G_c is 0 if $\varphi=1$.

For the interface condition, we consider the leading order of the fracture fluid stress, which is derived from the lubrication theory as established in [74, 75]. The effective fluid stress is given by $\sigma_F := \sigma|_{\Omega_F} = -p_F I$, where $p_F = p|_{\Omega_F}$ is the pressure in the fracture. As transmission conditions, we assume continuity of normal stresses:

$$\sigma^{por} \cdot \mathbf{n}_F = \sigma_F \cdot \mathbf{n}_F$$
 on $\Gamma_F \times (0, T)$,

or

$$(\sigma_R(\mathbf{u}) - \alpha p_R I) \cdot \mathbf{n}_F = -p_F \mathbf{n}_F \quad \text{on } \Gamma_F \times (0, T), \tag{6}$$

where \mathbf{n}_F is the outward pointing normal vector on Γ_F . In the following, we use the second transmission condition; namely, continuity of pressures:

$$p_R = p_F \quad \text{on } \Gamma_F \times (0, T).$$
 (7)

Consequently, we identify $p_R = p_F = p$ and obtain:

$$(\sigma_R(\mathbf{u}) - \alpha p I) \cdot \mathbf{n}_F = -p \mathbf{n}_F \quad \text{on } \Gamma_F \times (0, T). \tag{8}$$

Next, we follow [9] in which the stress tensor σ is additively decomposed as:

$$\sigma = \sigma_R = \sigma^+(\mathbf{u}) + \sigma^-(\mathbf{u})$$

into a tensile part $\sigma^+(\mathbf{u})$ and a compressive part $\sigma^-(\mathbf{u})$ by:

$$\sigma^{+}(\mathbf{u}) := \left(\frac{2}{d}G + \lambda\right)tr^{+}(e(\mathbf{u}))I + 2G(e(\mathbf{u}))$$
$$-\frac{1}{d}tr(e(\mathbf{u}))I), \tag{9}$$

$$\sigma^{-}(\mathbf{u}) := \left(\frac{2}{d}G + \lambda\right)tr^{-}(e(\mathbf{u}))I,\tag{10}$$

where

$$tr^{+}(e(\mathbf{u})) = \max(tr(e(\mathbf{u})), 0),$$

$$tr^{-}(e(\mathbf{u})) = tr(e(\mathbf{u})) - tr^{+}(e(\mathbf{u})).$$
(11)

Discussion of the different energy/stress splitting laws can be found in [6] and Section 2.2 in [16].

By utilizing the definition of φ , applying the interface conditions Eqs. 7–8, splitting Eqs. 9–10, and Gauss' divergence theorem (see Section 3.2 in [75]), we do not need to



distinguish between σ_R , p_R and σ_F , p_F , and we obtain the following global dissipation form:

$$E_{\varepsilon}(\mathbf{u}, p, \varphi) = \frac{1}{2} \int_{\Lambda} ((1 - \kappa)\varphi^{2} + \kappa)\sigma^{+}(\mathbf{u}) : \mathbf{e}(\mathbf{u})d\mathbf{x}$$

$$+ \frac{1}{2} \int_{\Lambda} \sigma^{-}(\mathbf{u}) : \mathbf{e}(\mathbf{u})d\mathbf{x}$$

$$- \int_{\partial \Lambda_{N}} (\tau + p\mathbf{n}) \cdot \mathbf{u}d\mathbf{s}$$

$$- \int_{\Lambda} \left((\alpha - 1)p - \alpha p_{R}^{0} \right) \varphi^{2} \nabla \cdot \mathbf{u}d\mathbf{x}$$

$$+ \int_{\Lambda} \varphi^{2} \nabla p \cdot \mathbf{u}d\mathbf{x}$$

$$+ G_{c} \int_{\Lambda} \left(\frac{1}{2\varepsilon} (1 - \varphi)^{2} + \frac{\varepsilon}{2} (\nabla \varphi)^{2} \right) d\mathbf{x}. (12)$$

Finally, we minimize the energy functional (12) with the following constraint, the irreversibility condition,

$$\partial_t \varphi \le 0,$$
 (13)

as in [71]. Thus, the phase field values decrease in time, which means only fracturing is allowed but not the bonding effect. Now that the problem becomes the following constrained optimization problem.

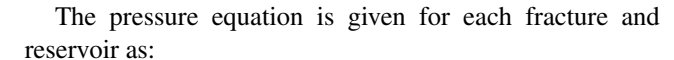
Problem 1 *Find* \mathbf{u} , p, φ *such that*

$$\min E_{\varepsilon}(\mathbf{u}, p, \varphi), \quad \text{subject to } \partial_t \varphi \leq 0.$$
 (14)

Mathematical derivation and analyses have been established in [74, 75]. Details of the numerical algorithms employed are discussed in Section 4.

3.2 Pressure diffraction system with two-phase flow in a fracture

We now introduce the pressure (flow) problem to solve for p in the previous section in terms of a diffraction system as described in [51, 74]. The fracture fluid is considered to be two-phase flow as established in [55]. However, we take account a single-phase fluid in porous media by assuming that only residing fluid in the fracture interacts on the fracture interface. Considering two-phase flow for both fracture and porous media is nontrivial due to the modeling choice of effective fluid stress and the pressure. In the pressure diffraction system, the underlying Darcy flow equations have the same structure in both the porous medium and the fracture. However, using the phase field indicator variable allows one to distinguish between reservoir flow and fracture flow as similar to the energy functional (5). To derive the flow pressure equations for each sub-domain, first we consider the two separate mass continuity equations for the fluid in the reservoir (Ω_R) and the fracture (Ω_F) .



$$\partial_t \left(\rho_j \phi_j^* \right) + \nabla \cdot (\rho_j \mathbf{v}_j) = q_j, \tag{15}$$

where $j = \{F, R\}$ indicates either fracture (F) or reservoir (R). The subscript R represents the variables defined in reservoir Ω_R , which is described with phase field function value $\varphi = 1$, and the subscript F represents the fracture region Ω_F where the phase field is $\varphi = 0$. Here, ρ_j , \mathbf{v}_j , and q_j are the fluid density, flux (velocity), and source term, respectively. In addition, ϕ_R^* is the effective porosity for the reservoir:

$$\phi_R^* := \phi_R^0 + \alpha \nabla \cdot \mathbf{u} + \frac{1}{M} \left(p_R - p_R^0 \right), \tag{16}$$

where M is Biot's modulus, and ϕ_R^0 is the initial porosity. The porosity in a fracture is set to be 1, i.e., $\phi_F^* = 1$. We assume that the fluid is slightly compressible and employ a linearized relation for the density:

$$\rho_{j} = \rho_{j}^{0} e^{c_{j} \left(p_{j} - p_{j_{0}} \right)}$$

$$\approx \rho_{j}^{0} \left[1 + c_{j} (p_{j} - \rho_{j}^{0}) \right], \quad (j = F, R), \quad (17)$$

where ρ_j^0 and c_j are the reference fluid density and fluid compressibility, respectively. The flux is described by Darcy's law, which is:

$$\mathbf{v}_{j} = -\frac{K_{j}}{\eta_{j}} \left(\nabla p_{j} - \rho_{j} \mathbf{g} \right), \tag{18}$$

where K_j is the permeability tensor, η_j is the fluid viscosity, and **g** is the gravitational acceleration. Thus, we can rewrite the equations for the pressure in the reservoir (15) by the following formulation:

Problem 2 *Find the pressure* p_R *such that:*

$$\partial_{t} \left(\frac{1}{M} p_{R} + \alpha (\nabla \cdot \mathbf{u}) \right) + \nabla \cdot \left(-\frac{K_{R}}{\eta_{R}} (\nabla p_{R} - \rho_{R} \mathbf{g}) \right)$$

$$= \frac{q_{R}}{\rho_{R}^{0}}, \text{ in } \Omega_{R} \times (0, T). \tag{19}$$

Next, we consider the fluid pressure in a fracture to be a two-phase flow as derived in [55]. Since the fracture flow becomes two phase, we split the pressure p_F by $p_{F,inj}$ and $p_{F,res}$, where $p_{F,res}$ is the pressure for residing fluid in a fracture and $p_{F,inj}$ is the pressure for the injection fluid in a fracture. In addition, we also have two variables for the saturation in a fracture denoted by $s_{F,res}$ (the saturation for the residing fluid) and $s_{F,inj}$ (saturation for the injection fluid). Note that a saturation variable is not defined in the reservoir since we assume a single-phase fluid. After employing the following relation:

$$s_{F,\text{inj}} + s_{F,\text{res}} = 1$$
 and $p_c = p_{F,\text{res}} - p_{F,\text{inj}}$, (20)



where p_c is referred as the capillary pressure in a fracture, we only solve for the saturation and the pressure of the injecting fluid, $s_{F,inj}$, $p_{F,inj}$ in a fracture.

The formations of pressure and saturation equation for two-phase flow in a fracture are given as:

Problem 3 Find the pressure $p_{F,ini}$ such that:

$$\partial_t (c_F p_{F,inj}) - \nabla \cdot \left(K_F \lambda_{tot} \nabla p_{F,inj} + K_F \lambda_{F,res} \nabla p_c(s_{F,inj}) \right)$$

$$= (q_F)_{tot} \text{ in } \Omega_F(t) \times (0,T),$$
(21)

where the total mobility, the mobility for the injecting fluid, and the mobility for the residing fluid are defined respectively:

$$\lambda_{tot} := \lambda_{tot}(s_{F,inj}) = \lambda_{F,inj}(s_{F,inj}) + \lambda_{F,res}(s_{F,inj}), \quad (22a)$$

$$\lambda_{F,inj} := \lambda_{F,inj}(s_{F,inj}) = \frac{k_{F,inj}(s_{F,inj})}{\eta_{F,inj}},$$
(22b)

$$\lambda_{F,res} := \lambda_{F,res}(s_{F,inj}) = \frac{k_{F,res}(s_{F,inj})}{\eta_{F,res}}, \text{ and}$$
 (22c)

$$(q_F)_{tot} := \frac{q_{F,inj}}{\rho_{F,inj}^0} + \frac{q_{F,res}}{\rho_{F,res}^0}.$$
 (22d)

Here, $\eta_{F,inj}$ is the injecting fluid viscosity; $k_{F,inj}$ and $k_{F,res}$ are the relative permeability for the injecting fluid and residing fluid, respectively. Moreover, $q_{F,inj} := \tilde{s}_{F,inj} \tilde{q}_{F,inj}$, where $\tilde{s}_{F,inj}, \tilde{q}_{F,inj}$ are the terms for saturation of injection/production fluid and amount of flow injection/production, respectively. If $\tilde{q}_{F,inj} > 0$, $\tilde{s}_{q,inj}$ is the injected saturation of the fluid and if $\tilde{q}_{F,inj} < 0$, $\tilde{s}_{q,inj}$ is the produced saturation. We note that $\tilde{s}_{q,inj} + \tilde{s}_{q,res} = 1$.

Problem 4 Find the saturation of the injected fluid $s_{F,inj}$ such that:

$$\begin{split} \partial_t s_{F,inj} - \nabla \cdot \left(K_F \frac{k_{F,inj}(s_{F,inj})}{\eta_{F,inj}} \nabla p_{F,inj} \right) &= q_{F,inj} \ in \ \Omega_F \times (0,T), \ (23a) \\ K_F \frac{k_{F,inj}(s_{F,inj})}{\eta_{F,inj}} \nabla p_{F,inj} \cdot \mathbf{n}_F &= 0 \quad on \ \Gamma_F(t) \times (0,T). \ (23b) \end{split}$$

The above coupled Formulations 3 and 4 are similar to the two-phase flow model in porous media as discussed in [10, 25, 32, 43, 60], but here we employ the following relative permeabilities derived in [55, Chapter 3] to consider two-phase flow in a fracture. The relative permeabilities are given as:

$$k_{F,\text{res}}(s_{F,\text{inj}}) := \frac{1}{2} (1 - s_{F,\text{inj}})^2 (2 + s_{F,\text{inj}}),$$

$$k_{F,\text{inj}}(s_{F,\text{inj}}) := s_{F,\text{inj}}^3 + \frac{3s_{F,\text{inj}}(1 - s_{F,\text{inj}}^2)}{2}.$$
(24)

In addition, by following the approach from [11], we use the simplified capillary pressure defined as:

$$p_c(s_{F,\text{inj}}) = ((k_{F,\text{res}}(s_{F,\text{inj}}))^{-1/2} + (k_{F,\text{inj}}(s_{F,\text{inj}}))^{-1/2})(1 - s_{F,\text{inj}}).$$
(25)

Finally, from Formulation 2 and coupled Formulation 3–4, we formulate the pressure diffraction system with the indicator phase field variable φ .

Problem 5 *Find the pressure p such that:*

$$\theta \,\partial_t \, p - \nabla \cdot (K_{\text{EFF}} \nabla \, p) = \bar{q},\tag{26}$$

where

$$\theta := \chi_{R}(\varphi) \frac{1}{M} + \chi_{F}(\varphi) c_{F}, \quad K_{\text{EFF}} := \chi_{R}(\varphi) \frac{K_{R}}{\eta_{R}}$$

$$+ \chi_{F}(\varphi) (K_{F} \lambda_{tot})$$

$$\bar{q} := \chi_{R}(\varphi) \left(\frac{q_{R}}{\rho_{R}^{0}} - \alpha \partial_{t} (\nabla \cdot \mathbf{u}) \right) + \chi_{F}(\varphi) ((q_{F})_{tot}$$

$$+ \nabla \cdot (K_{F} \lambda_{F, \text{res}} \nabla p_{c}(s_{F, \text{inj}})) \right).$$

In formulation 5, formulations 2 and 3, the reservoir and fracture flow equations, are coupled through the indicator functions $\chi_R(\varphi)$ and $\chi_F(\varphi)$, which are defined as:

$$\chi_F(\varphi) = \frac{1 - H^*(\varphi)}{2}, \quad \chi_R(\varphi) = \frac{1 + H^*(\varphi)}{2}, \tag{27}$$

where H^* is a regularization of the sign functions expressed

$$H^*(a) = \begin{cases} 1 & \text{for } a > 0.5 + D_{\varepsilon} \\ -1 & \text{for } a > 0.5 - D_{\varepsilon} \\ \frac{a - 0.5}{D_{\varepsilon}} & \text{otherwise.} \end{cases}$$
 (28)

Thus, the phase field function is utilized as an indicator function, which is similar to the energy functional (12). Here, we set $D_{\epsilon}=0.1$ throughout this paper. Except for the case where D_{ϵ} approaches 0, the choice of D_{ϵ} does not influence the results of pressure significantly as illustrated for the single-phase flow in [62].

Finally, the pressure diffraction system (formulation 5) is supplemented with initial and boundary conditions. The initial conditions are given by:

$$p(\mathbf{x}, 0) = p^0$$
 and $s_{F, \text{inj}}(\mathbf{x}, 0) = s_{F, \text{inj}}^0$ for all $\mathbf{x} \in \Omega_R(t = 0)$,

where p^0 and $s_{F,\text{inj}}^0$ are smooth given initial pressure and saturation, respectively. The boundary and interface conditions for pressure are described as:

$$K_R \nabla p_R \cdot \mathbf{n} = 0$$
 on $\partial \Lambda \times (0, T)$, (29a)

$$p_R = p_F \text{ res}$$
 on $\Gamma_F \times (0, T)$, (29b)

$$\frac{K_R}{\eta_R} \nabla p_R \cdot \mathbf{n}_F = \frac{K_F k_{F, \text{res}}}{\eta_{F, \text{res}}} \nabla p_{F, \text{res}} \cdot \mathbf{n}_F \text{ on } \Gamma_F \times (0, T), \quad (29c)$$

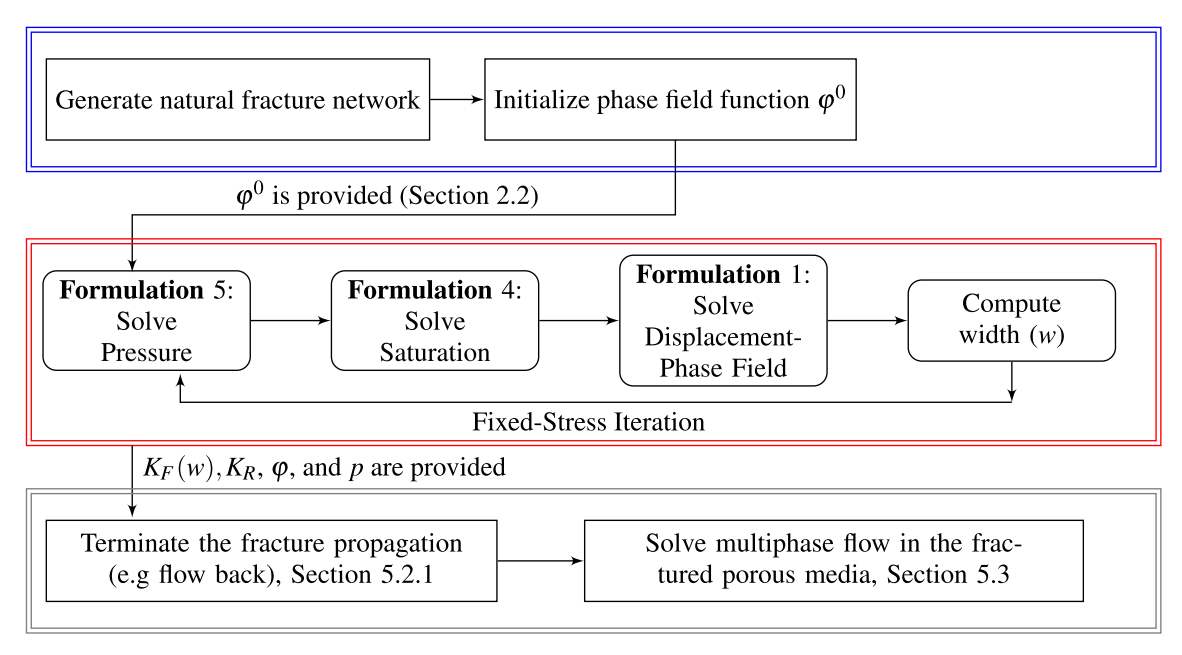


Fig. 5 The global algorithm flowchart

3.3 Computation of the fracture width

For the pressure diffraction system described in the previous section, the permeability for the fracture is defined as:

$$K_F := K_F(w) = \frac{w(\mathbf{u})^2}{12},$$
 (30)

where $w(\mathbf{u})$ denotes the fracture aperture (crack opening displacement), which is computed as a jump of the normal direction of displacement. As shown in [96, 101], the classical lubrication law has a cubic power of the width but we lose one order and arrive at a quadratic law by dividing the flux over the cross-sectional area of the fracture [74]. For accurate width computations of non-planar fractures, an

additional algorithm is required as discussed in [28, 61, 77]. The definition of the width reads:

$$2w(\mathbf{u}) = -[\mathbf{u} \cdot \mathbf{n}_F],$$

which is the jump of the normal displacements, where \mathbf{n}_F is the unit normal on the crack surface (Γ_F) . Robust approximation of the \mathbf{n}_F for non-planar fractures is not trivial, but here we employ the efficient algorithm by using the phase field variable.

First, we define the isoline φ_{LS} , which is simply obtained from the phase field variable φ by:

$$\varphi_{LS} := \varphi - C_{LS}. \tag{31}$$

To compute φ_{LS} , $C_{LS} \in (0, 1)$ is a constant chosen for defining the fracture boundary Γ_F . Throughout this paper

Fig. 6 Example 1: a setup for investigating interactions between natural fractures and a hydraulic fracture; b illustrates the phase field presentation for this setup

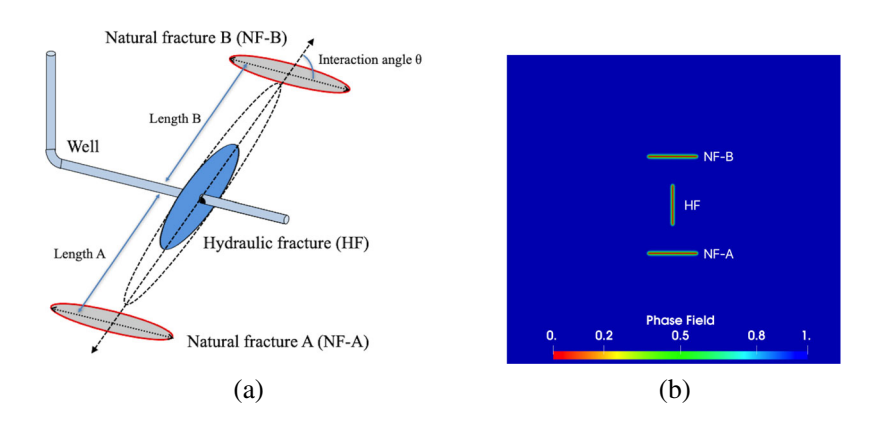
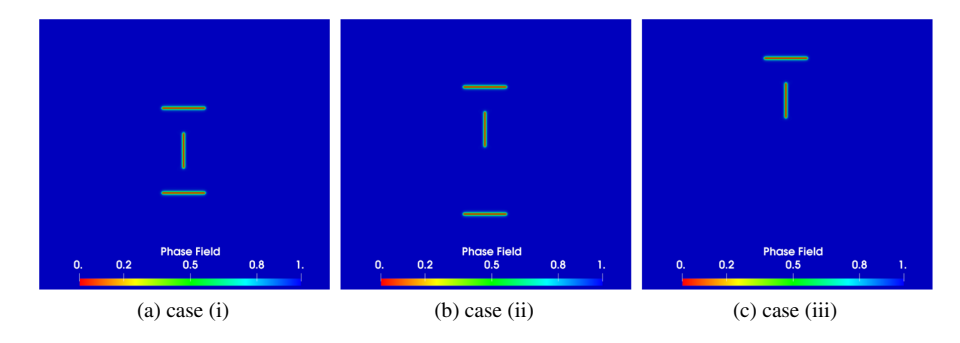




Fig. 7 Example 1: Setup for three different cases with different positions for the natural fractures (top and bottom) but the hydraulic fracture is fixed at the middle



for simplicity, we set $C_{LS}=0.1$. We now define Γ_F as the zero level set of a function φ_{LS} such that:

$$\Gamma_F := \{ \mathbf{x} \in \Lambda \mid \varphi_{\mathsf{LS}} = 0, \ \varphi(\mathbf{x}, t) = C_{LS} \}.$$

and

$$\Omega_R := \{ \mathbf{x} \in \Lambda \mid \varphi_{\mathsf{LS}} > 0, \varphi(\mathbf{x}, t) > C_{LS} \}, \text{ and}$$

$$\Omega_F := \{ \mathbf{x} \in \Lambda \mid \varphi_{\mathsf{LS}} < 0, \varphi(\mathbf{x}, t) < C_{LS} \}.$$

Then, the width can be approximated by:

$$\mathbf{u} \cdot \mathbf{n}_F \approx \mathbf{u} \cdot \frac{\nabla \varphi_{LS}}{\|\nabla \varphi_{LS}\|}.$$

In order to improve the fracture width representation inside the fracture, we finally solve a crack width interpolation problem; see [61] (therein Formulation 6 and Fig. 4). More details of the algorithm are provided in [61, 77].

4 Numerical algorithm and discretizations

Overall, we are solving the following equations: a displacement/phase field energy minimization problem, a pressure diffraction problem with two-phase flow in a fracture, a saturation problem, and a crack width problem.

The nonlinear displacement/phase field system (Formulation 1) is solved with Newton's method and line search algorithms. The constraint minimization problem is treated with a semi-smooth Newton method, so-called a primal-dual active set method [41]. A robust and efficient iteration

Fig. 8 Example 1 case (i): phase field values for propagating fractures for each time step n

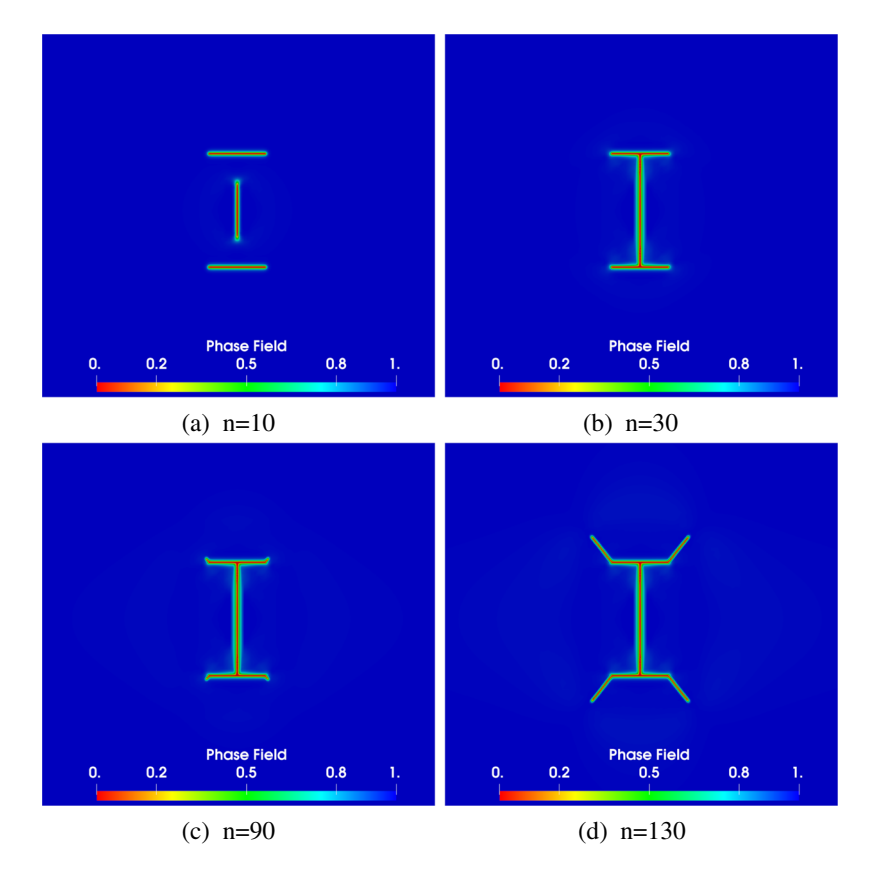




Fig. 9 Example 1 case (i): Pressure values for propagating fractures for each time step n. We observe the pressure drop from \mathbf{a} to \mathbf{b} , after the hydraulic fracture encounters the natural fractures. Then, additional pressure is required \mathbf{c} to restart propagation from the tip of the natural fractures. \mathbf{d} Moreover, the pressure decreases when the fracture starts to propagate then it increases again

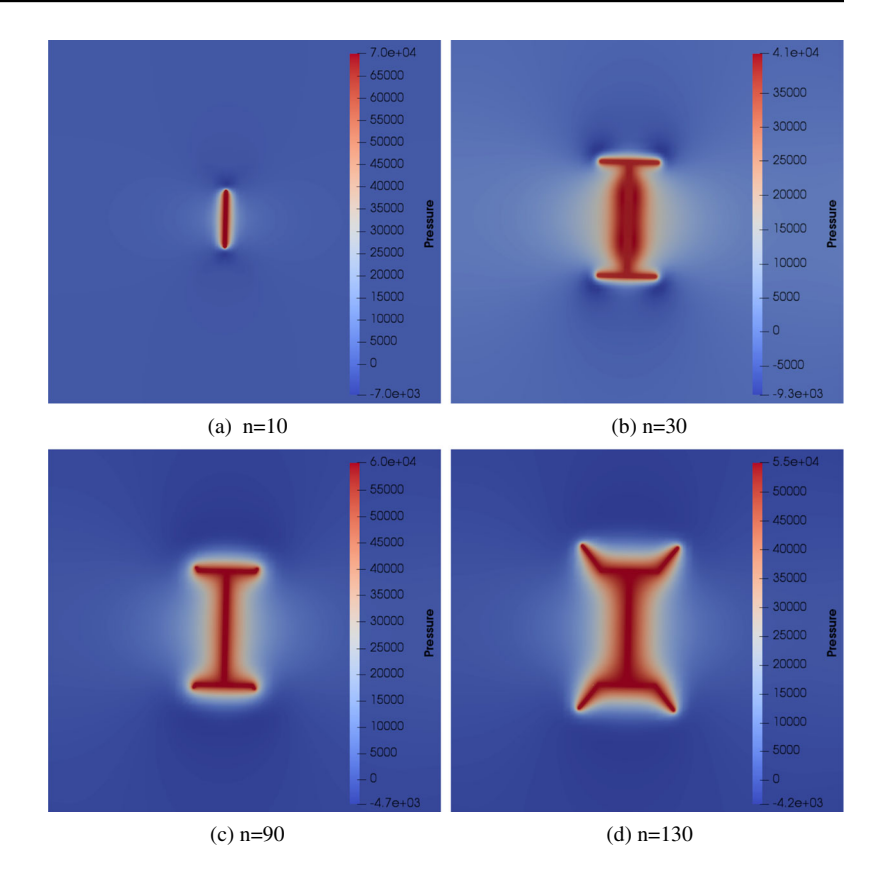


Fig. 10 Example 1 case (ii): Phase field values for each time step n

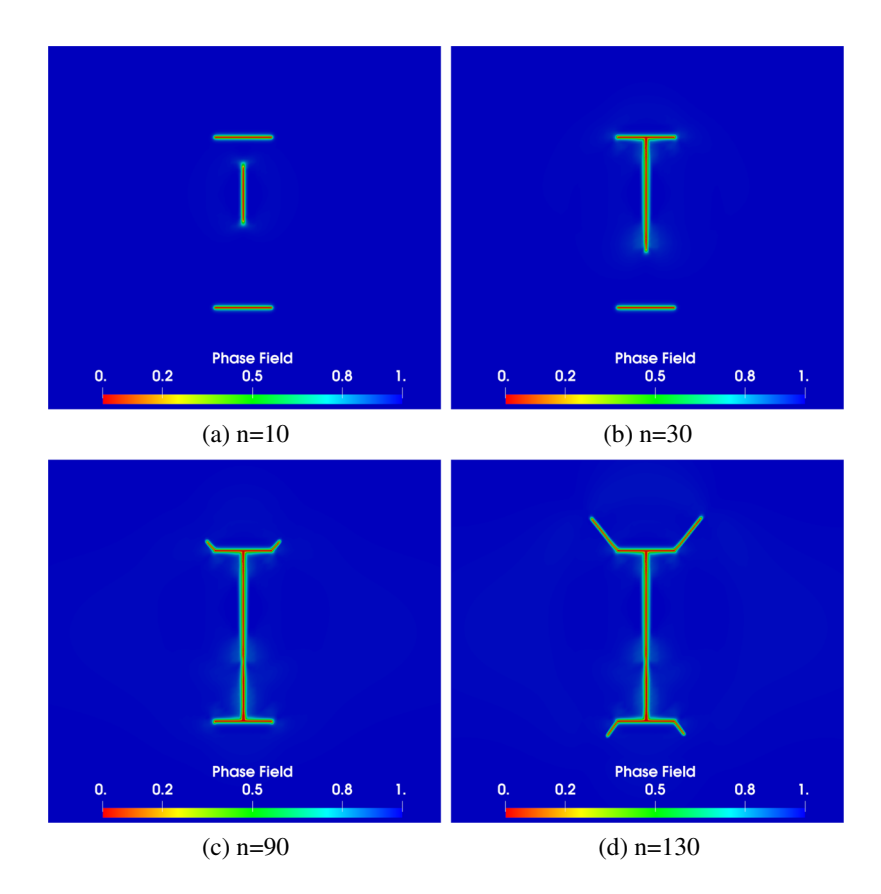




Fig. 11 Example 1 case (ii): Pressure values for propagating fractures for each time step n

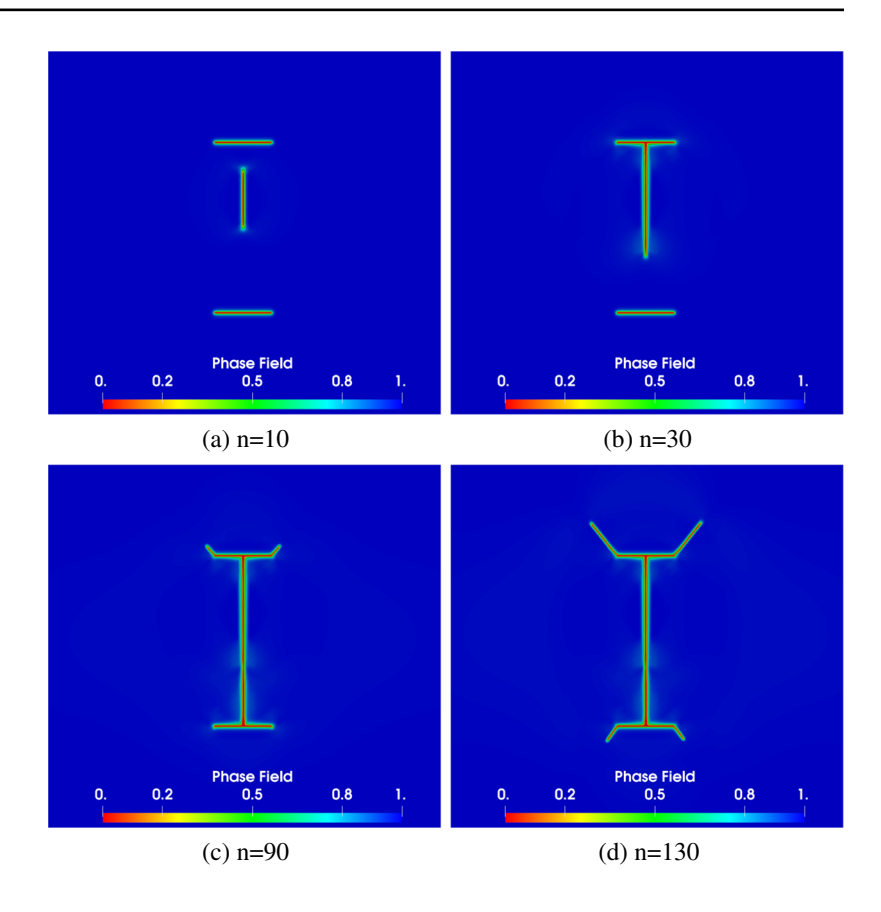


Fig. 12 Example 1 case: Phase field values for each time step n

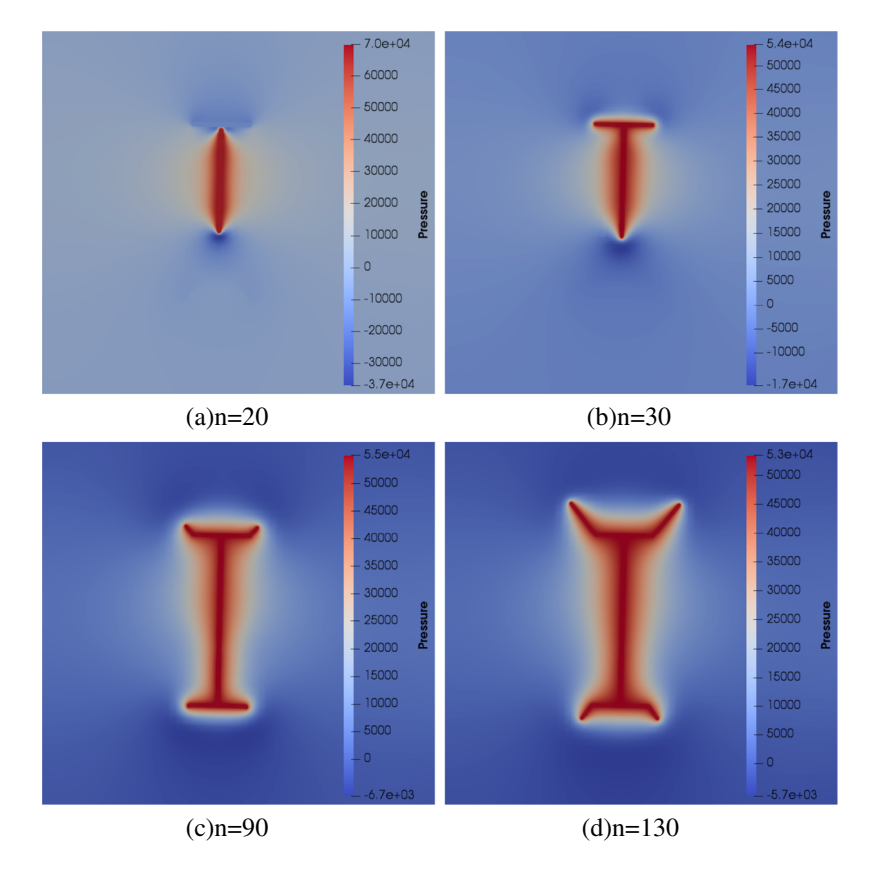
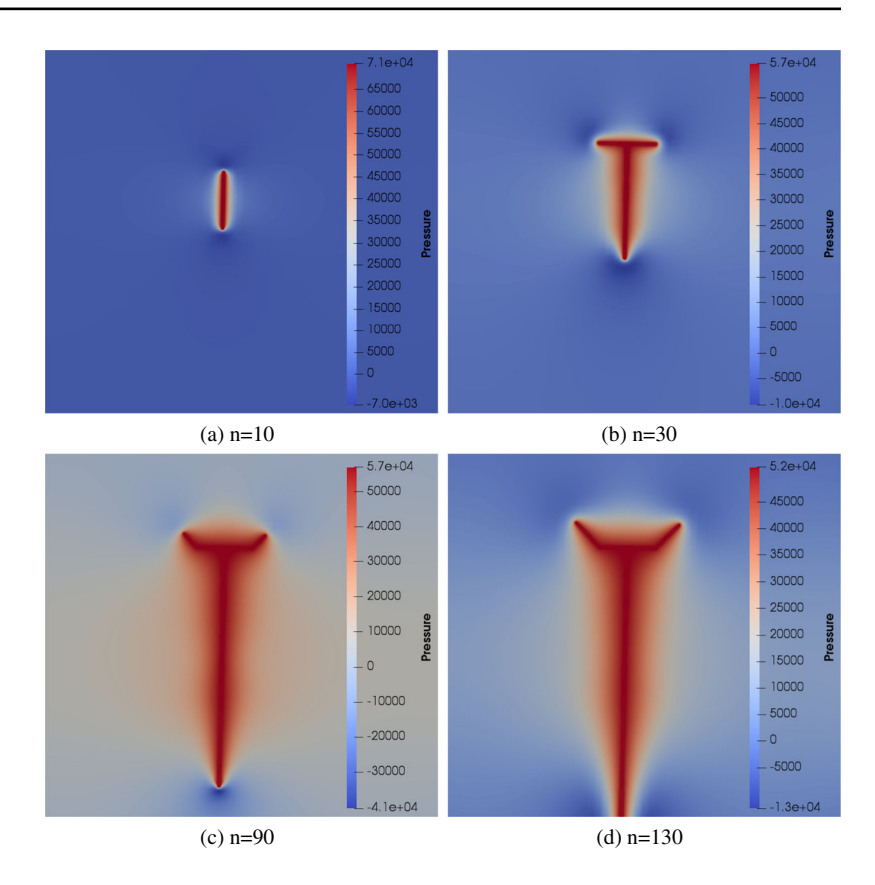




Fig. 13 Example 1 case (iii): Pressure values for propagating fractures for each time step n

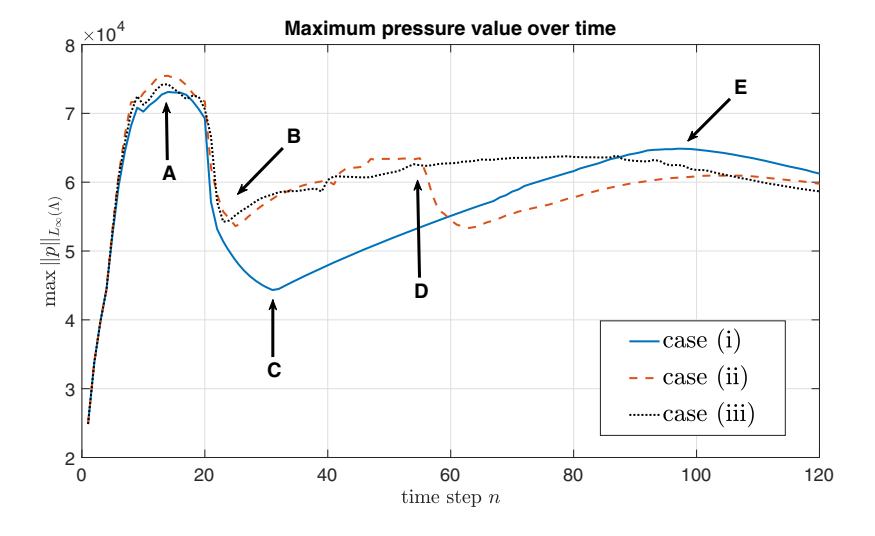


scheme for the system is outlined in [39] with more details. The linear equation systems in Newton's iteration are solved with GMRES solvers and diagonal block-preconditioning from Trilinos [40] solver. This quasi-static system is discretized by continuous Galerkin (CG) finite element methods.

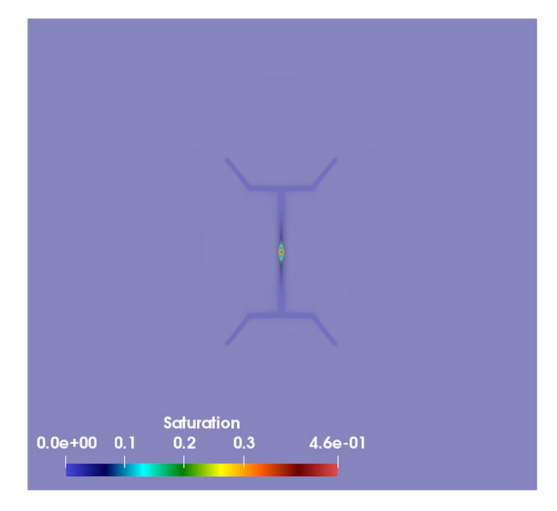
For the Formulations 4 and 5, enriched Galerkin (EG) finite element methods [54, 88] are utilized for both the

pressure and saturation equations in order to obtain local mass conservation. It is well known that the flow should be locally mass conservative to avoid unphysical spurious oscillations, especially when the flow is coupled with the transport system (saturation) [60, 82]. The EG method is formulated by adding discontinuous constant to continuous Galerkin finite element methods. The discretized bilinear form is the same as classical discontinuous Galerkin (DG)

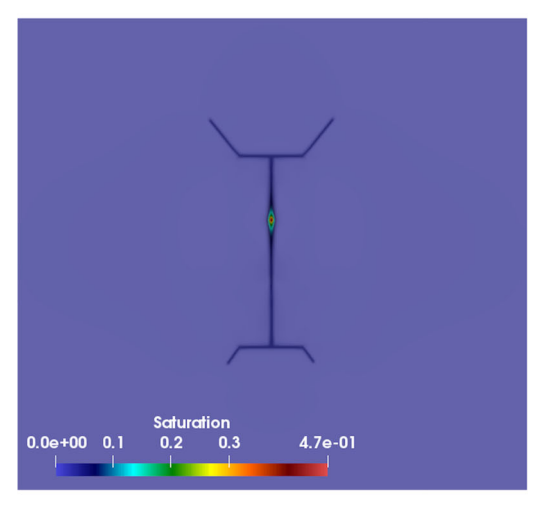
Fig. 14 Example 1: The maximum pressure profile $\|p\|_{L_{\infty}(A)}$ over time for each cases







(a)case(i)



(b)case(ii)

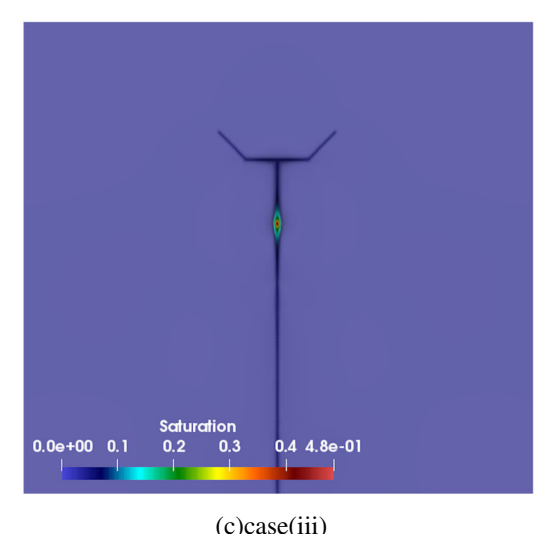


Fig. 15 Example 1: Saturation values each case at n = 130

finite element methods but the degree of freedom of EG is fewer than that of DG. Thus, EG inherits the advantages of DG but has less computational time. Recently, EG is employed for various multiphysics applications with dynamic mesh adaptivity [26, 46, 59]. The pressure and saturation diffraction problems are solved with generalized minimal residual method (GMRES) solvers with diagonal block preconditioning. An iterative Implicit Pressure Explicit Saturation (IMPES) formulation is employed for coupling Formulations 4 and 5.

Next, coupling flow (pressure and saturation) and geomechanics (displacement/phase field), i.e., Formulations 1 and 5, is based on a fixed-stress iteration algorithm. The fixed-stress iteration is well known in subsurface modeling, environmental, and petroleum engineering problems [23, 49, 50, 72, 73, 83, 84]. For detailed explanations and numerical demonstrations using fixed-stress iteration for the phase field fracture, we refer to [61]. A theoretical justification of the fixed-stress phase field fracture scheme in which the phase field values are assumed to be given has been recently shown in [3]. Some alternative approaches, for example, fixed-point iterations for either flow or poroelasticity with the phase field fracture has been recently studied in [21].

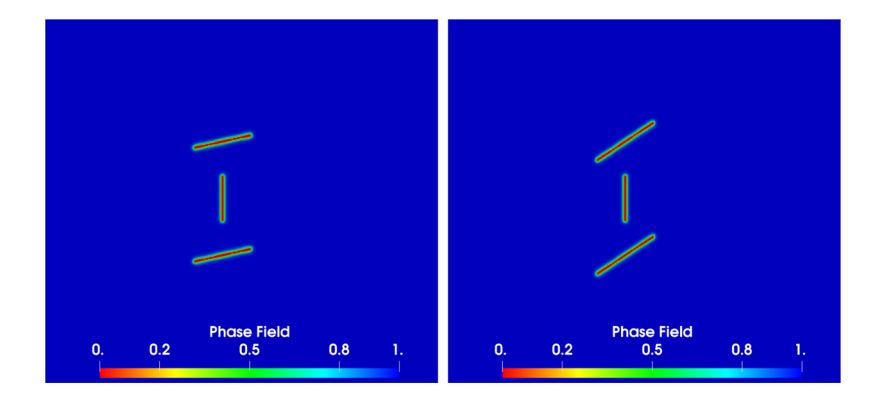
In Fig. 5, the overall framework for the numerical simulation stages are illustrated. First, the phase field function is initialized to describe natural fracture networks as discussed in Section 2.2. Then, two-phase flow is injected to selected fractures for fracture propagation. Finally, a couple of post-processing procedures are possible in our proposed algorithm. The pressure and fracture width values after terminating the fracture propagation can be studied, and this is known as flowback. In addition, general wetting and non-wetting two-phase flow models in porous media, such as production process, can be simulated with given permeability values in the fractured porous media.

5 Numerical examples

Our objective is to develop a reliable and efficient computational framework that can handle realistic field applications which involve natural fracture network and multiphase fluid-filled fracture propagation. The presented algorithm has been implemented based on the finite element library deal.II [4] and MPI parallel programming developed in [39, 62], and referred to IPACS (Integrated Phase field Advanced Crack Simulator) [93]. In this final section, we present numerical examples to illustrate the capabilities of IPACS and to demonstrate the effectiveness of the proposed algorithm.



Fig. 16 Example 2: Setup of natural fractures and a hydraulic fracture with different interaction angles θ . With our definition in Fig. 6(a), the interaction angle of case (iv) θ_{iv} is larger than the interaction angle of case (iv) θ_{v} , i.e., $\theta_{iv} > \theta_{v}$



5.1 Interactions between natural fractures and a two-phase fluid-filled hydraulic fracture

In this section, we investigate the interactions between natural fractures and a two-phase fluid-filled fracture propagation. A schematic setup for the numerical experiments is illustrated in Fig. 6 and is based on the well-known studies of Olson and Wu [97]. The findings of our scheme are well aligned with the results of the latter. We remark that many studies have been carried out addressing interactions between natural and simulated fractures based on similar configurations and applying various techniques discussed

in the introduction for single-phase flow. We emphasize that our phase field Biot model and the variational energy minimization approach does not require additional criterion or physical assumption to be defined for joining, branching, and interactions of these fractures and can handle two-phase flow. These features for interaction between fractures are already embedded in the variational energy minimization approach.

In our numerical experiments, we vary the natural fracture configuration by changing the lengths A and B, and the interaction angle between the hydraulic fracture (HF) and the natural fractures (NF). Then, fracture geometry, pressure

Fig. 17 Example 2 case (iv).: Phase field values for each time step n

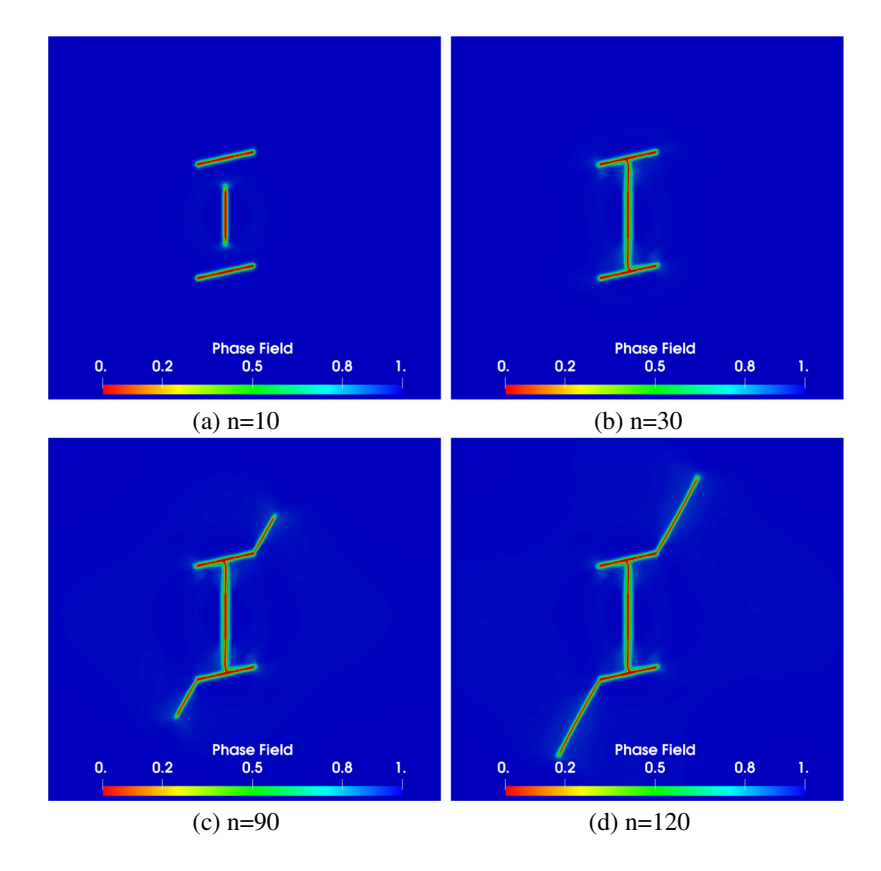




Fig. 18 Example 2 case (iv): Fracture width values for each time step n

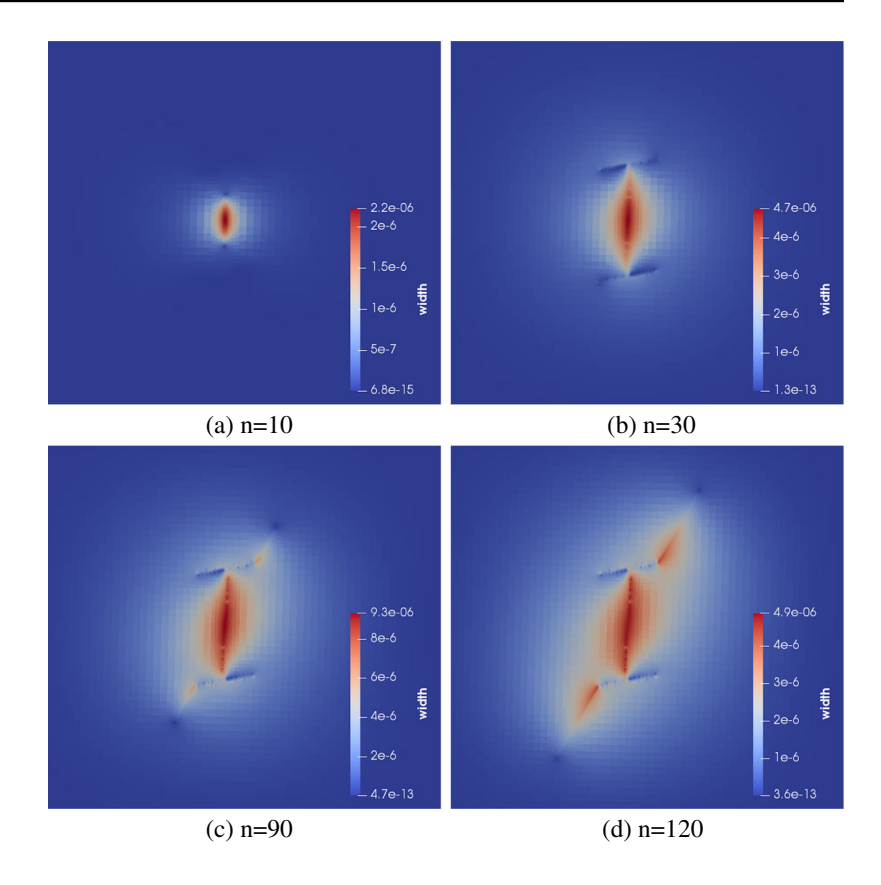


Fig. 19 Example 2 case (iv): Pressure values for propagating fractures for each time step n

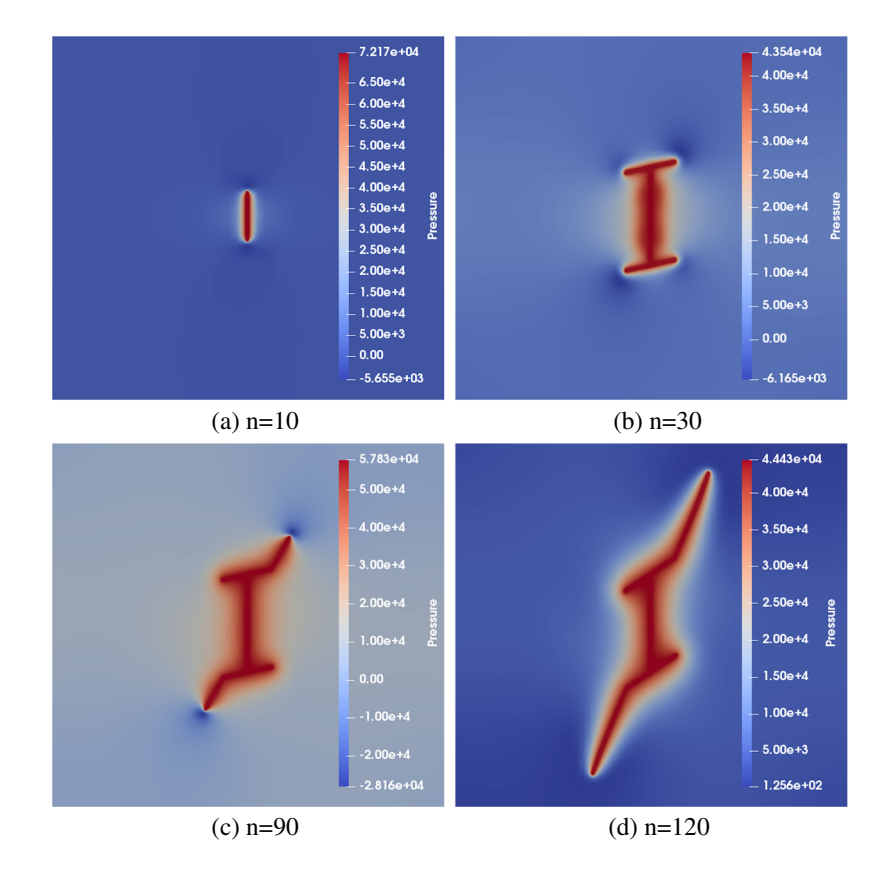




Fig. 20 Example 2 case (v): Phase field values for propagating fractures for each time step *n*

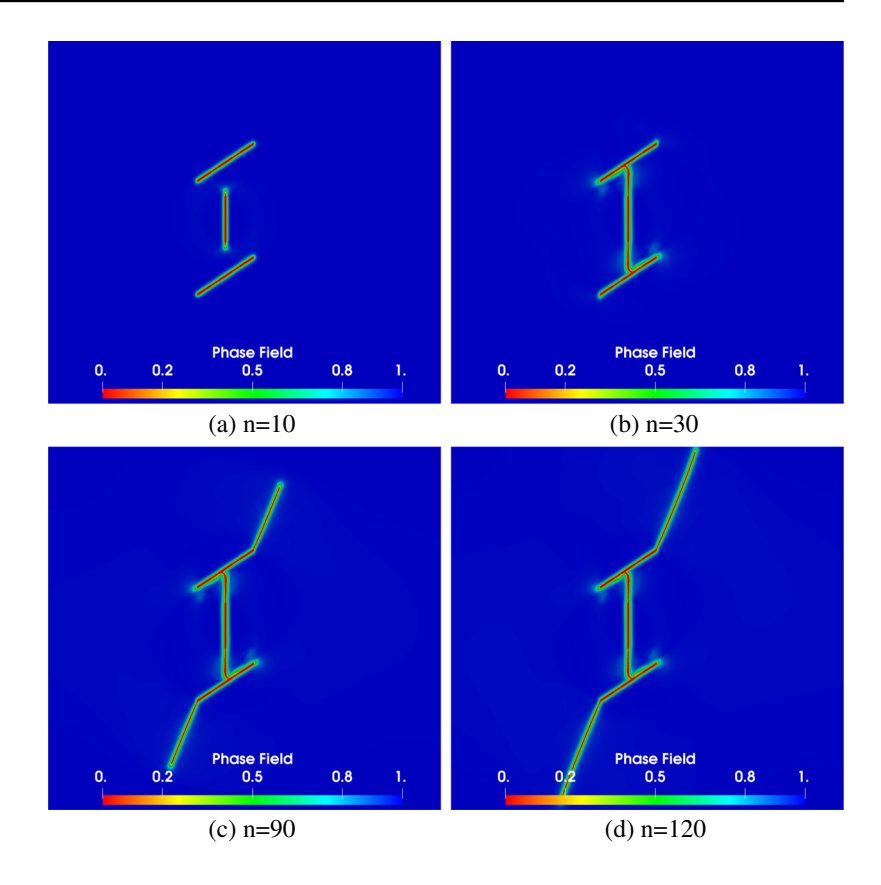


Fig. 21 Example 2 case (v): Fracture width values for propagating fractures for each time step *n*

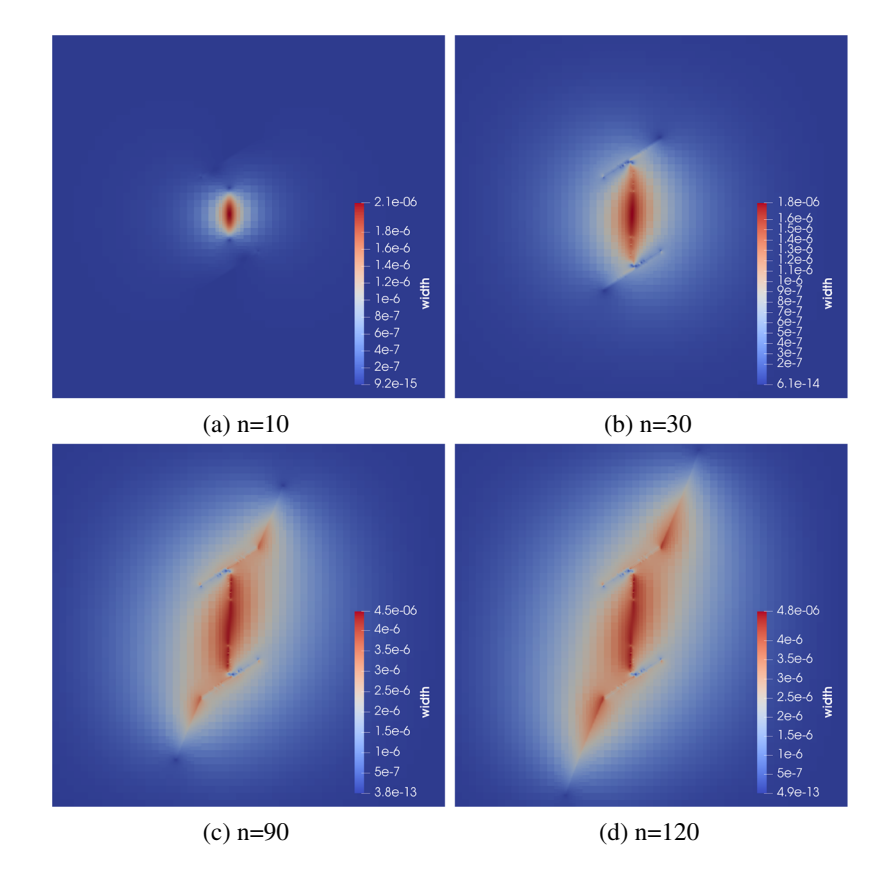
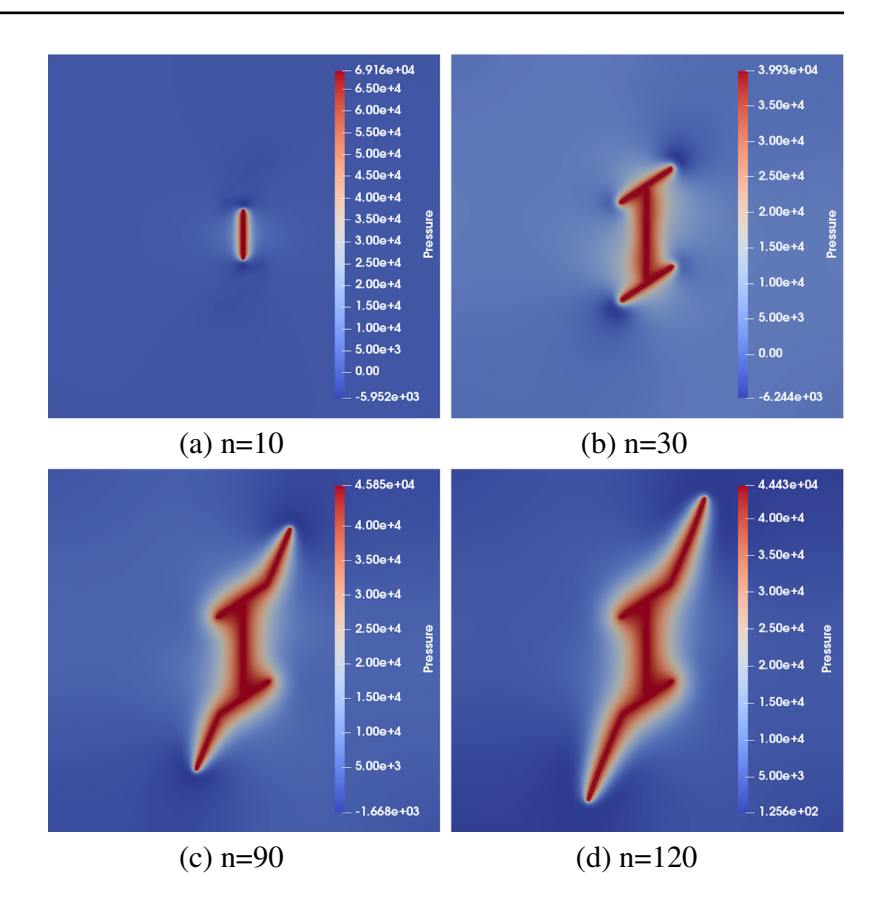




Fig. 22 Example 2 case (v): Pressure values for propagating fractures for each time step n



distribution, and fracture aperture (width) will be compared and discussed for each case.

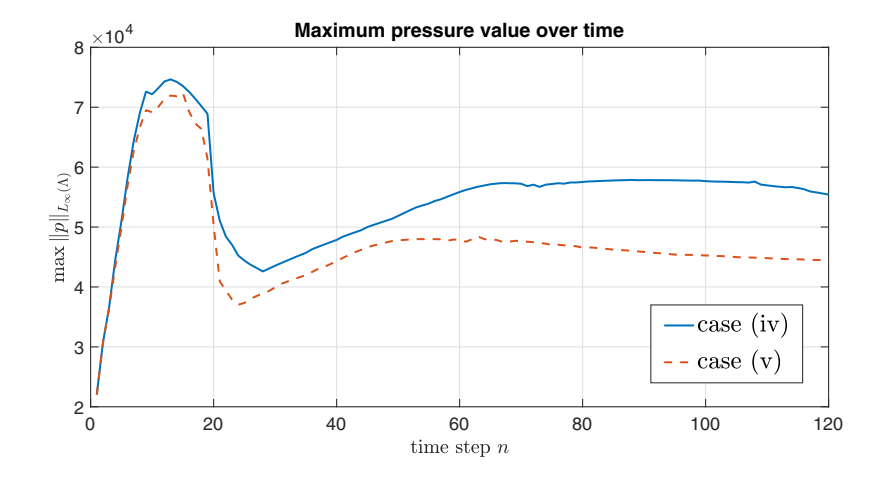
5.1.1 Numerical parameters

For this example, the computational domain is defined as $\Lambda = (0\text{m},4\text{m})^2$ and a initial fractures are positioned with half length $l_0 = 0.2$ m and half height, h_{\min} . Here, h_{\min} is the minimum size of the spatial discretization h (mesh size for the finite element method). The initial mesh is 7 times

uniformly refined and 3 more levels are refined near the fracture interface with the predictor-corrector mesh refinement algorithm [39]. Here, the criteria for the predictor-corrector refinement is chosen as $\phi=0.8$; thus, the mesh with the phase field values below 0.8 will be refined up to three times more than the initial refinement level.

In all of our computational results, the length of the phase field diffusive zone is set to be $\varepsilon=2h_{min}$ and so the initial thickness of phase field variable φ is $2h_{min}$, and we set the regularization parameter as $\kappa=10^{-10}\times h_{min}$. The time

Fig. 23 Example 2: The maximum pressure profile $\|p\|_{L_{\infty}(\Lambda)}$ over time for each different case. We observe the larger pressure values with the larger interaction angle (case (iv)) due to smaller fracture width values





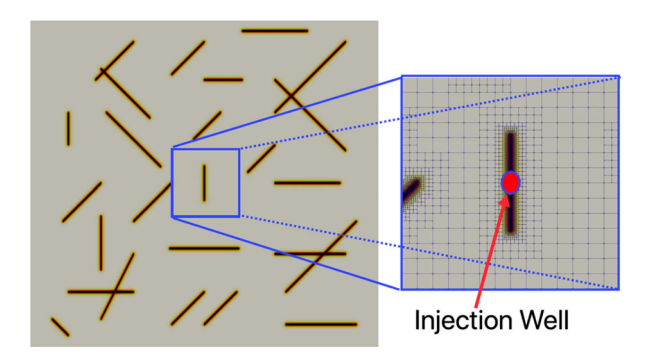


Fig. 24 Example 3: **a** setup of the initial phase field representing natural fractures and a hydraulic fracture. The darker region indicates the fracture area with the phase field value $\varphi=0$; **b** a hydraulic fracture is placed at the middle of the domain and the pressure will be injected from the center. In addition, the adaptive mesh refinement near the fracture is shown

step size is chosen as $\delta t = 0.01$ and here $h_{min} = 0.0056$ m. Furthermore, Biot's coefficient is $\alpha = 1$, the wellbore pressure is $q_F = 10$ m³/s and $M = 1 \times 10^8$ Pa, $c_F = 1 \times 10^{-8}$ Pa. The viscosities are chosen as $v_R = v_F = 1 \times 10^{-3}$ Ns/m². The reservoir permeability is $K_R = 1d$. The densities are $\rho_F^0 = 1$ kg/m³. The critical energy release rate is chosen as $G_C = 10$ Nm⁻¹, Young's modulus is $E = 10^8$ Pa, and Poisson ratio is set to v = 0.2.

For the displacements, we prescribe homogeneous Dirichlet conditions on $\partial \Lambda$. For the phase field and the pressure system, homogeneous Neumann conditions are employed. The initial phase field values are set to 0 for the initial fracture described above and $\varphi=1$ otherwise. Also, the initial displacement and pressure values are set to 0.

5.1.2 Example 1: The effects of different lengths between natural and hydraulic fractures

First, we simulate three different cases as shown in Fig. 7 by varying the position of natural fractures, i.e., changing the lengths A and B. Here, the interaction angle is fixed as $\theta = 90^{\circ}$. The location of the midpoint of the hydraulic fracture (injection point) is (2m, 2m). Case (i) has two natural fractures symmetrically placed with the lengths A and B both set as 0.5 m; case (ii) keeps the length B as

Fig. 25 Example 3: Phase field values for propagating fractures for each time step n. Each A, B, and C denotes the joining of the hydraulic fracture with natural fractures

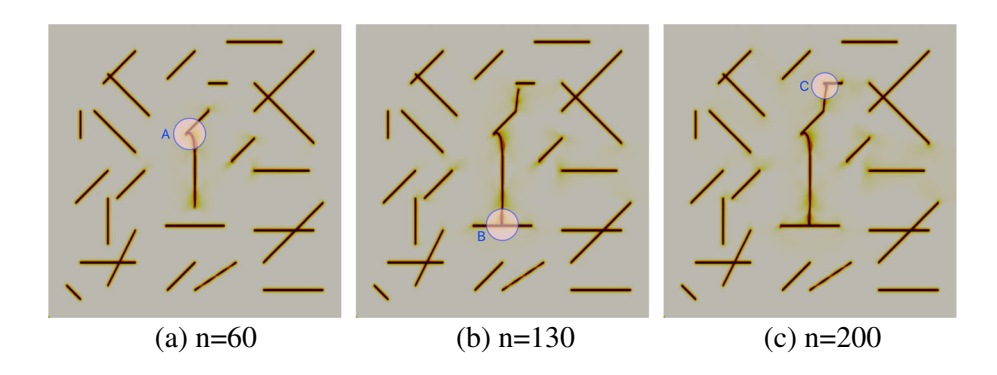
0.5 m but the length A is set as 1.0 m, and in case (iii), only one natural fracture (NF-B) exists with length B equal to 0.5 m. Figures 7, 8, 9, 10, 11, 12, 13, 14 and 15 illustrate the detailed comparison of phase field and pressure values for each of the test cases.

Case (i) Phase field values for propagation fracture in case (i) for each time step *n* are presented in Fig. 8. As the setup is symmetric, the propagation of the fracture is also symmetric. Compared with the fracture propagation speed from Fig. 8a to b, it takes a much longer time to initiate the branching of the fractures at the tip of the natural fractures in Fig. 8c.

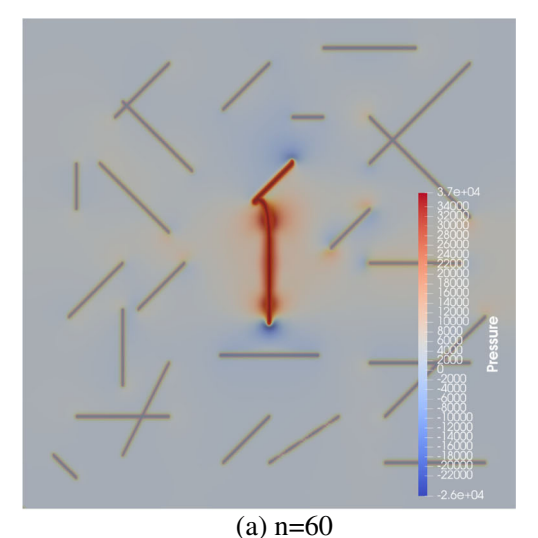
The main reason for the difference in propagation speed is due to the pressure drop when the hydraulic fracture meets and joins with the natural fractures. This effect is depicted in Fig. 9, and the results show that additional pressure needs to be injected to initiate hydraulic fractures branching from the tip of natural fractures.

Case (ii) In this case, the set up is non symmetric and one natural fracture (NF-A) is farther than another natural fracture (NF-B). Thus, as shown in Fig. 10, the hydraulic fracture joins sequentially with these existing fractures. When the hydraulic fracture first joins the closest natural fracture (Fig. 10b), the fracture propagation speed gets slower than the speed of the fracture tip propagating in the opposite direction with no intersection.

Figure 11 illustrates the pressure distribution for each time step in case (ii). We observe a similar phenomenon as case (i) that the pressure drops when fracture propagation initiates and the hydraulic fracture interacts with the natural fractures (see Fig. 11a, b). While the one tip of hydraulic fracture intersects with the natural fracture, the pressure distribution is almost steady since the injection fluid still flows into the other tip for the hydraulic fracture propagation. It is easier for the hydraulic fracture to continue propagating to the direction where it could avoid the natural fracture. However, if the tip of hydraulic fracture at the other side also joins the other natural fracture (NF-A), then the pressure within the fracture will start build up and propagation speed in this side will be slowed down.







3,1e+04 -28000 -28000 -28000 -28000 -18000 -

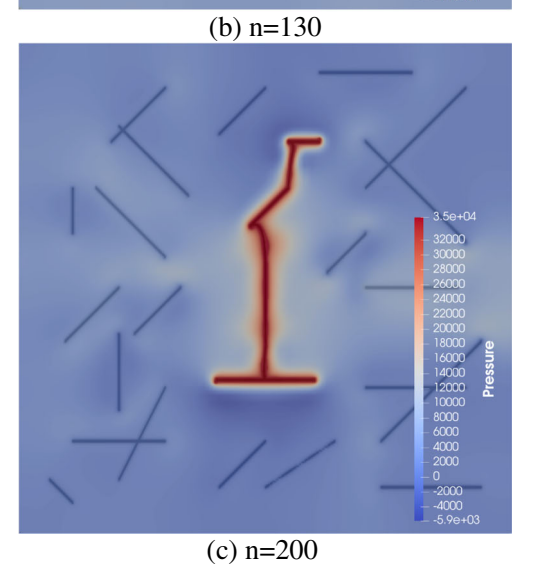


Fig. 26 Example 3: Pressure values for propagating fractures for each time step n

Case (iii) With only one natural fracture (NF-B), we observe that the fracture propagation speed of the tip with no natural fracture side is faster than the tip with the interaction (Fig. 12c). In addition, we observe the branching of the fractures from the side tip of the natural fracture is slower than case (ii) since the pressure tends to propagate the fracture to the opposite direction. Figure 13 provides the pressure profile for each time step.

Overall, Fig. 14 compares the maximum pressure value $(\max \|p\|_{L_2(\Lambda)})$, which is almost the value near the injection point, over time for the above three different cases. First, for the all three cases, the pressure drops when the fracture propagation is initiated (point A in Fig. 14). The amount of the pressure drop for case (i) is larger than for the two other cases, since in case (i) the propagating fracture intersects two NFs at the same time and the pressure becomes distributed. Case (ii) has two pressure drops A and D in Fig. 14 and the propagating fracture intersects the NF sequentially. After the pressure drops, the pressure slowly builds up in the fractures to initiate branching and deflecting the fracture propagation at the end of the natural fracture. As we observe in case (i), the pressure drop occurs again when branching of the fracture starts (see E in Fig. 14). Thus, using the pressure profile, one can observe that the injection pressure could be employed as an indicator for detecting the joining/interactions of hydraulic fractures with natural fractures.

Saturation values of the injected fluid at the time step n=120 are illustrated in Fig. 15. Here we are utilizing permeabilities derived in [55] and it is observed that due to the very low permeability in the porous media and the small width values, the injected fluid is pushing the residing fluid to propagate the fractures in our modeling.

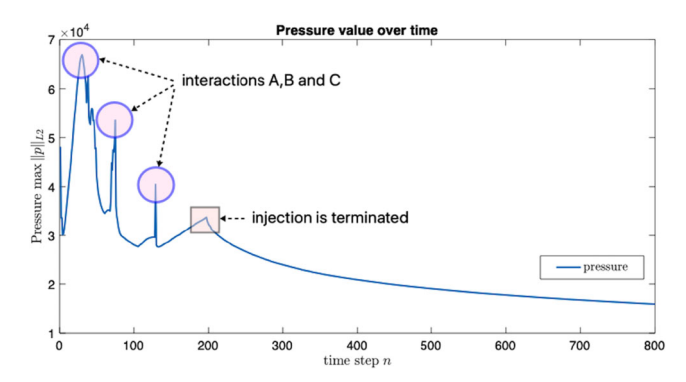
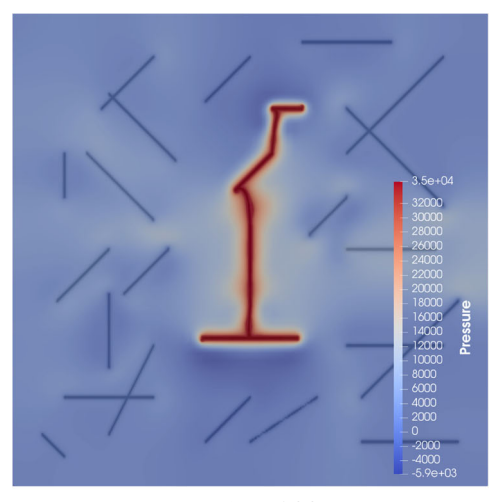
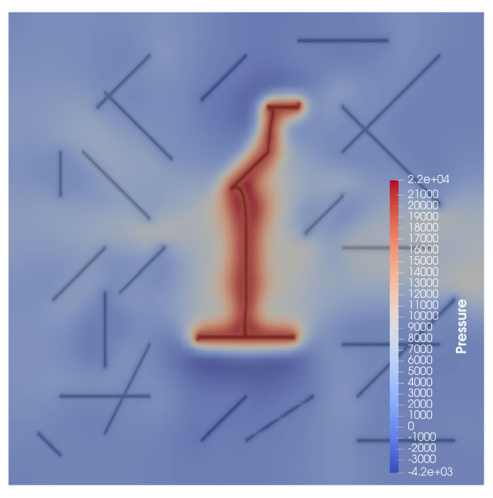


Fig. 27 Example 3: The maximum pressure profile $||p||_{L_{\infty}(\Lambda)}$ over time including the termination of the injection



(a) n=200



(b) n=400

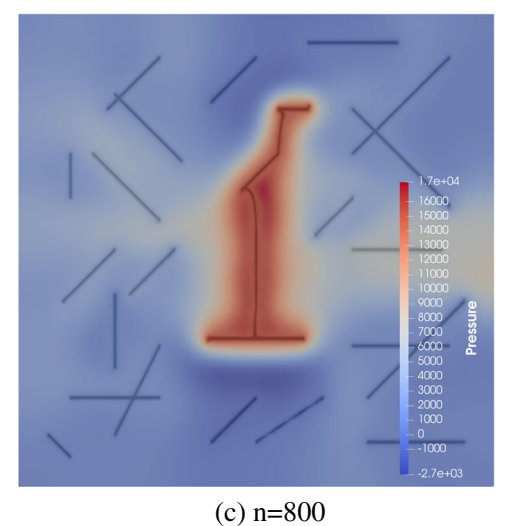


Fig. 28 Example 3: Pressure values after the termination of the

injection at time step n = 200

5.1.3 Example 2: The effects of different interaction angles between natural and hydraulic fractures

We have observed in the previous section that both sides of the natural fracture branched when the intersection angle $\theta = 90^{\circ}$. However, it is generally more natural for the angles to depend on their orientation [35, 52]. Thus, in this section, we investigate the effects of the angles joining natural and hydraulic fractures. See Fig. 16 for a description of the cases considered. Figures 17, 18, and 19 illustrate phase field, fracture width, and pressure values, respectively for the case (iv). In addition, Figs. 20, 21, and 22 presents the phase field, fracture width, and the pressure values, respectively for the case (v).

One of the major difference of cases (iv) and (v) compared with the previous cases (i), (ii), and (iii) where $\theta=90^\circ$ is that branching of natural fractures is only activated in one side. See Figs. 17d and 20d. In addition, Figs. 18 and 21 illustrate the width values for each time step for case (iv) and case (v), respectively. It is clearly shown that only one side of the natural fracture branches due to the smaller width values on the other side of the natural fracture. Moreover, the natural fractures with smaller interaction angle branch farther than the larger interaction angle.

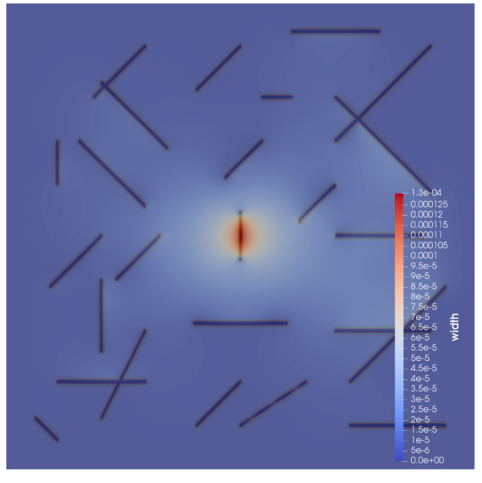
By comparing the difference of the width values between cases (iv) and (v), we observe that the fracture width opening is smaller with the larger interaction angle (θ_{iv}) than the smaller interaction angle (θ_{v}). Thus, case (iv) has smaller fracture opening displacement (width) values than case (v). Moreover, higher pressure values for the larger interaction angle are observed in Figs. 19 and 22. Figure 23 illustrates the maximum pressure value over time. This difference is related to the width values.

We note again that the numerical results presented in Examples 1 and 2 are well aligned with the results discussed in Olson and Wu [97]. However, we emphasize that our phase field approach based on the energy minimization approach does not require any additional criterion to be defined near the crack tip for these interactions of the fractures. These features for interaction between fractures are already embedded in the variational energy minimization approach [47].

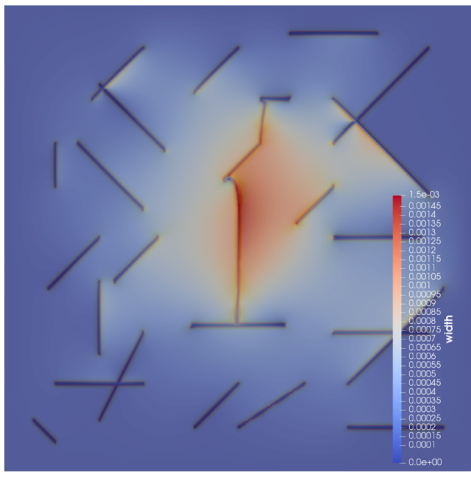
5.2 Example 3: Fracture propagation in diffusive natural fracture network

A major goal of the fracking process is to select the location of the injection wells for maximizing the fractures sites in order to increase production in an environmentally prudent fashion [57]. A possible approach is to apply simulation to





(a) n=10



(b) n=200

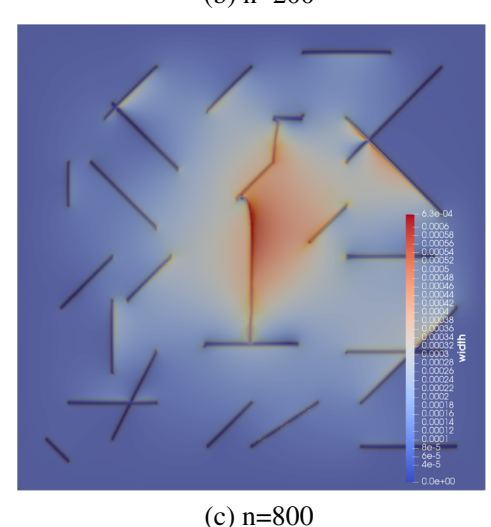


Fig. 29 Example 3: Width values for each time step n. The maximum width value decreases after terminating the injection, i.e., (c) has smaller maximum width values than (b)

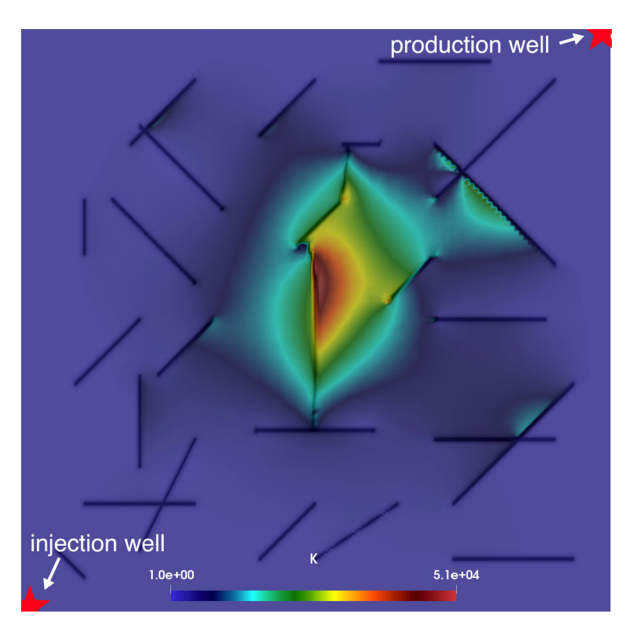


Fig. 30 Example 4: The computed permeability field is illustrated with the fractures from the previous example. Also, injection and production wells are placed

connect with natural fractures that can be utilized effectively and safely. In this section, we consider a setup with approximately 25 natural fractures to study the effects of the network and this is a novel result that emphasizes the capability of our diffusive fracture approach. Here, the natural fractures are defined as discussed in Section 2.2 for the diffusive zone phase field approach. The hydraulic fracture is placed at the middle of the domain 20 m, 20 m with initial length as $l_0 = 4$ m and stimulated using our two-phase fluid-filled fracturing model (Fig. 23). See Fig. 24 for a description. The commutation domain is $\Lambda = (0 \text{ m}, 40 \text{ m})^2$ with $h_{\min} = 0.04$ m, and other numerical parameters are equivalent with the previous examples.

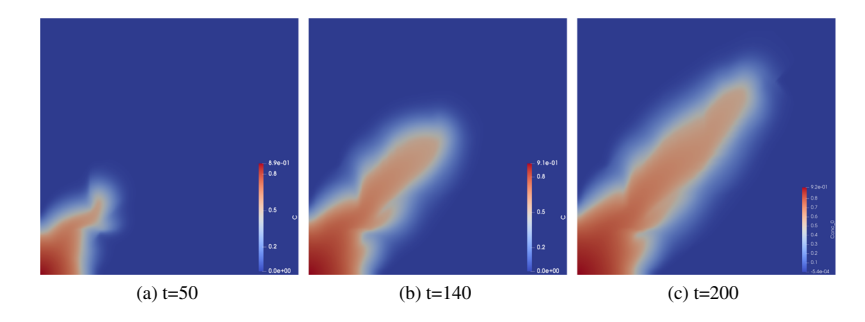
Figure 25 illustrates the propagation of the hydraulic fracture and the interaction with natural fracture for each time step. Three interactions with the hydraulic fracture and natural fractures are denoted as A, B, and C in the figure. Figure 26 presents the corresponding pressure values while the fractures are stimulated. In addition, Fig. 27 presents the maximum pressure values over the entire time. We observe three pressure drops (A, B, and C), which indicates the joining of the hydraulic fracture with natural fractures.

5.2.1 After termination of injecting the fluid: Flowback

Following the hydraulic fracturing process, the fluids that returned to the surface within a specified length of time are referred to as flowback. Since hydraulic fractures are



Fig. 31 Example 4: saturation value of the wetting phase from the injection well to the production well at each time *t*



filled with fracturing fluid before flowback, quantitatively analyzing early time flow rate and pressure allows one to obtain properties of induced fractures which complements production data, and provides insight into the effectiveness of the fracturing. Thus, it is important to investigate post-fracturing water flowback [1, 2, 29, 33]. Flowback control has been extensively studied by the petroleum industry with several field tests including Marcellus, Fayetteville, and Barnett formations in the USA [2, 37].

Thus, to investigate the flowback process in our simulation studies, we stop the injection of the fluid at time step number n=200 and we observe the pressure profile after the termination of injection. In Fig. 27, we clearly note that the pressure is decreasing after the termination at n=200. Also, Fig. 28 illustrates the pressure values after the termination of the injection and we remark that the pressure values tend to equilibrium.

Recent studies indicate that post-treatment fracture flow-back procedures during closure are often critical to the retention of fracture conductivity near the wellbore [13, 81]. Figure 29 illustrates the width values for the fractures at (a) the early time of the injection n = 10, (b) just before the termination of the injection n = 200, and (c) the final time step n = 800. Although the phase field approach for the fracture propagation does not allow the complete closure of the fracture due to the irreversibility condition (13), we can still observe the decrease in the width values. More advanced flowback studies with the presented computational framework is currently being considered by the authors.

5.3 Example 5: Two-phase flow in the fractured porous media

The scenario in this example is that the production simulations are performed after the hydraulic fracturing. The permeability field for the fractured porous media is computed by using the width values provided from the previous section. Thus, the permeability is derived by employing the relation (30), where the width values are given from Fig. 29 at time step n = 800. See Fig. 30 for the setup with the production and injection wells.

The two-phase flow and transport model described in [60] are employed here and we set the wetting phase

pressure and saturation (s_w) as the primary variables. In the same computational domain, 0 m, 40 m)² as the previous example, wells are rate specified at the corners with injection at (0 m, 0 m) and production at (40 m, 40 m). The lowest permeability is $K_D = 1\text{D}$. We assume the domain is saturated with a non-wetting phase, i.e., $s_n^0 = 1$ and $s_w^0 = 0$, and a wetting phase fluid is injected. The viscosities for wetting phase and non-wetting phase are 1cp and 3cp, respectively, and the densities for wetting phase and non-wetting phase are 1000 kg/m^3 and 830 kg/m^3 , respectively. The injection and production rates are 2.5 m/s and -2.5 m/s, respectively. The minimum mesh size is h = 0.44 and the time step is 0.1. For simplicity, the relative permeabilities for wetting phase (k_w) and non-wetting phase (k_n) are given as a function of the wetting phase saturation (s_w) :

$$k_w(s_w) := s_w^2$$
, and $k_n(s_w) := (1 - s_w)^2$. (32)

See [60, Section 4] for more details about the numerical parameters and the algorithm.

Figure 31 illustrates the saturation value of the wetting phase from the injection well to the production well. We observe that the flow direction and speed are affected by the fractures. These results can provide useful information to the re-fracturing process. We note that the production process after stimulation involves treatment of complicated scenarios with the injection and the production wells. Considering these cases requires a fully coupled multiphase Biot system with an appropriate pore pressure and realistic data set.

6 Conclusion

A computational framework, utilizing a phase field approach for coupling two-phase flow, geomechanics, and fracture propagation in porous media was presented. Our numerical experiments centered on investigating the interactions between natural and stimulated fractures. Our studies included the effects arising from different lengths of the fractures, different intersection angles, and fracture networks. We observed that fluid-filled fracture propagation in naturally fractured porous media leads to joining and branching of stimulated fractures into natural fractures and



their interactions. Injection pressure decreases when the fluid-filled fracture meets natural fractures. Here, pressure needs to build up for continuation of branching and propagation. Although dependent on many factors, pressure can be employed as an indicator of natural fractures. In addition, we considered the closure of fractures and flowback processes after termination of injection and noted pressure decreasing and tending to equilibrium. Post-treatment of fracture flowback is important for retention of fracture conductivity around the wellbore. Although the phase field approach does not allow the complete closure of the fracture due to an irreversibility condition, we observed decreases in width values after complex closure of the fractures. Our computational framework allows coupling with a general multiphase production model. While the above studies assumed a two-phase model, ongoing work involves adding a gas phase and consideration of realistic field models.

Acknowledgments The authors thank to Andro Mikelić, Thomas Wick, and Mohamad Jammoul for their support and assistance with this project. S. Lee wants to thank the support from the Center for Subsurface Modeling at the Oden Institute for Computational Engineering and Sciences at the University of Texas at Austin.

Acknowledgments S. Lee is partially supported by the National Science Foundation under Grant No. (NSF DMS-1913016).

References

- Abbasi, M., Dehghanpour, H., Hawkes, R.V.: Flowback Analysis for Fracture Characterization. In: SPE Canadian Unconventional Resources Conference. Society of Petroleum Engineers (2012)
- Alkouh, A., McKetta, S., Wattenbarger, R.A.: Estimation of effective-fracture volume using water-flowback and production data for shale-gas wells. J. Can. Pet. Technol. 53(05), 290–303 (2014)
- Almani, T., Lee, S., Wheeler, M., Wick, T.: Multirate Coupling for Flow and Geomechanics Applied to Hydraulic Fracturing Using an Adaptive Phase-Field Technique. SPE RSC 182610-MS, Feb. 2017, Montgomery, Texas, USA (2017)
- Alzetta, G., Arndt, D., Bangerth, W., Boddu, V., Brands, B., Davydov, D., Gassmoeller, R., Heister, T., Heltai, L., Kormann, K., Kronbichler, M., Maier, M., Pelteret, J.P., Turcksin, B., Wells, D.: The deal.II library, version 9.0. J. Numer. Math. 26(4), 173–183 (2018). https://doi.org/10.1515/jnma-2018-0054
- Ambati, M., Gerasimov, T., De Lorenzis, L.: Phase-field modeling of ductile fracture. Comput. Mech. 55(5), 1017–1040 (2015)
- Ambati, M., Gerasimov, T., De Lorenzis, L.: A review on phasefield models of brittle fracture and a new fast hybrid formulation. Comput. Mech. 55(2), 383–405 (2015)
- Ambrosio, L., Tortorelli, V.: Approximation of functionals depending on jumps by elliptic functionals via γ-convergence. Comm. Pure Appl. Math. 43, 999–1036 (1990)
- Ambrosio, L., Tortorelli, V.: On the approximation of free discontinuity problems. Boll. Un. Mat. Ital. B 6, 105–123 (1992)
- Amor, H., Marigo, J.J., Maurini, C.: Regularized formulation of the variational brittle fracture with unilateral contact: Numerical experiments. Journal of Mechanics Physics of Solids 57, 1209– 1229 (2009)

- Arbogast, T., Juntunen, M., Pool, J., Wheeler, M.F.: A discontinuous Galerkin method for two-phase flow in a porous medium enforcing H (div) velocity and continuous capillary pressure. Comput. Geosci. 17(6), 1055–1078 (2013)
- Babchin, A., Faybishenko, B.: On the capillary pressure function in porous media based on relative permeabilities of two immiscible fluids. Colloids Surf. A Physicochem. Eng. Asp. 462, 225–230 (2014)
- 12. Barenblatt, G.: The Mathematical Theory of Equilibrium Cracks in Brittle Fracture, pp. 55–129. Elsevier, Amsterdam (1962)
- Barree, R.D., Mukherjee, H.: Engineering criteria for fracture flowback procedures. In: Low Permeability Reservoirs Symposium. Society of Petroleum Engineers (1995)
- Biot, M.: General theory of three-dimensional consolidation. J. Appl. Phys. 12(2), 155–164 (1941)
- Biot, M.: Mechanics of deformation and acoustic propagation in porous media. J. Appl. Phys. 33, 14–82 (1962)
- Borden, M.J., Verhoosel, C.V., Scott, M.A., Hughes, T.J.R., Landis, C.M.: A phase-field description of dynamic brittle fracture. Comput. Methods Appl. Mech. Eng. 217, 77–95 (2012)
- Bourdin, B., Chukwudozie, C., Yoshioka, K.: A variational approach to the numerical simulation of hydraulic fracturing. SPE Journal Conference Paper 159154-MS (2012)
- Bourdin, B., Francfort, G., Marigo, J.J.: Numerical experiments in revisited brittle fracture. Journal of the Mechanics and Physics of Solids 48(4), 797–826 (2000)
- Bourdin, B., Francfort, G., Marigo, J.J.: The variational approach to fracture. J. Elasticity 91(1–3), 1–148 (2008)
- Bourdin, B., Marigo, J.J., Maurini, C., Sicsic, P.: Morphogenesis and propagation of complex cracks induced by thermal shocks. Phys. Rev. Lett. 112, 014301 (2014)
- Brun, M.K., Wick, T., Berre, I., Nordbotten, J.M., Radu, F.A.: An iterative staggered scheme for phase field brittle fracture propagation with stabilizing parameters. Computer Methods in Applied Mechanics and Engineering 361, 112752 (2020). https://doi.org/10.1016/j.cma.2019.112752. http://www.sciencedirect.com/science/article/pii/S0045782519306425
- Cajuhi, T., Sanavia, L., De Lorenzis, L.: Phase-field modeling of fracture in variably saturated porous media. Computational Mechanics (2017)
- Castelletto, N., White, J.A., Tchelepi, H.A.: Accuracy and convergence properties of the fixed-stress iterative solution of two-way coupled poromechanics. Int. J. Numer. Anal. Methods Geomech. 39(14), 1593–1618 (2015)
- Chai, Z., Yan, B., Killough, J., Wang, Y.: An efficient method for fractured shale reservoir history matching: The embedded discrete fracture multi-continuum approach. J. Pet. Sci. Eng. 160, 170–181 (2018)
- Chen, Z., Huan, G., Ma, Y.: Computational methods for multiphase flows in porous media. SIAM (2006)
- Choo, J., Lee, S.: Enriched galerkin finite elements for coupled poromechanics with local mass conservation. Comput. Methods Appl.Mech. Eng. 341, 311 –332 (2018)
- Choo, J., Sun, W.: Cracking and damage from crystallization in pores: Coupled chemo-hydro-mechanics and phase-field modeling. Comput. Methods Appl. Mech. Eng. 335, 347–379 (2018)
- Chukwudozie, C., Bourdin, B., Yoshioka, K.: A variational phase-field model for hydraulic fracturing in porous media. Comput. Methods Appl. Mech. Eng. 347, 957–982 (2019)
- Crafton, J.W., Gunderson, D.W.: Stimulation flowback management–keeping a good completion good. In: SPE Annual Technical Conference and Exhibition. Society of Petroleum Engineers (2007)
- Dahi-Taleghani, A., Olson, J.E., et al.: Numerical modeling of multistranded-hydraulic-fracture propagation: accounting for the interaction between induced and natural fractures. SPE journal 16(03), 575–581 (2011)



- Delorme, M., Bossie-Codreanu, D., Ben-Gharbia, I., Khebzegga, O., Khebzegga, N., Ricois, O., et al.: Unconventional production forecast needs integration of field hydraulic stimulation data through fracture model calibration and optimized numerical scheme. In: SPE Argentina Exploration and Production of Unconventional Resources Symposium. Society of Petroleum Engineers (2016)
- El-Amin, M.F., Kou, J., Sun, S., Salama, A.: An iterative implicit scheme for nanoparticles transport with two-phase flow in porous media. Procedia Computer Science 80, 1344–1353 (2016)
- 33. Ezulike, O., Dehghanpour, H., Virues, C., Hawkes, R.V., Jones Jr, R.S.: Flowback fracture closure: a key factor for estimating effective pore volume. SPE Reservoir Evaluation & Engineering 19(04), 567–582 (2016)
- Francfort, G., Marigo, J.J.: Revisiting brittle fracture as an energy minimization problem. J. Mech. Phys. Solids 46(8), 1319–1342 (1998)
- 35. Gale, J.F., Reed, R.M., Holder, J.: Natural fractures in the barnett shale and their importance for hydraulic fracture treatments. AAPG bulletin **91**(4), 603–622 (2007)
- Griffith, A.: The phenomena of rupture and flow in solids. Philos. Trans. R. Soc. Lond. 221, 163–198 (1921)
- Haluszczak, L.O., Rose, A.W., Kump, L.R.: Geochemical evaluation of flowback brine from marcellus gas wells in Pennsylvania, Usa. Appl. Geochem. 28, 55–61 (2013)
- Heider, Y., Markert, B.: A phase-field modeling approach of hydraulic fracture in saturated porous media. Mechanics Research Communications 80, 38–46 (2017). Multi-Physics of Solids at Fracture
- Heister, T., Wheeler, M.F., Wick, T.: A primal-dual active set method and predictor-corrector mesh adaptivity for computing fracture propagation using a phase-field approach. Comput. Methods Appl. Mech. Engrg. 290, 466–495 (2015)
- Heroux, M., Bartlett, R., Hoekstra, V.H.R., Hu, J., Kolda, T., Lehoucq, R., Long, K., Pawlowski, R., Phipps, E., Salinger, A., Thornquist, H., Tuminaro, R., Willenbring, J., Williams, A.: An overview of trilinos. Tech. Rep. SAND2003-2927 Sandia National Laboratories (2003)
- Hintermüller, M., Ito, K., Kunisch, K.: The primal-dual active set strategy as a semismooth newton method. SIAM J. Optim. 13(3), 865–888 (2002)
- HosseiniMehr, M., Cusini, M., Vuik, C., Hajibeygi, H.: Algebraic dynamic multilevel method for embedded discrete fracture model (f-adm). J. Comput. Phys. 373, 324–345 (2018)
- 43. Hoteit, H., Firoozabadi, A.: Numerical modeling of two-phase flow in heterogeneous permeable media with different capillarity pressures. Adv. Water Resour. **31**(1), 56–73 (2008)
- Jacobs, T.: To solve frac hits, unconventional engineering must revolve around them. https://www.spe.org/en/jpt/jpt-articledetail/?art=5089 (2019)
- Jammoul, M., Ganis, B., Wheeler, M.: General semi-structured discretization for flow and geomechanics on diffusive fracture networks. In: SPE Reservoir Simulation Conference. Society of Petroleum Engineers (2019)
- Kadeethum, T., Nick, H., Lee, S., Richardson, C., Salimzadeh, S., Ballarin, F.: A novel enriched galerkin method for modelling coupled flow and mechanical deformation in heterogeneous porous media. In: 53rd US Rock Mechanics/Geomechanics Symposium. American Rock Mechanics Association, New York, NY, USA (2019)
- Karma, A., Kessler, D.A., Levine, H.: Phase-field model of mode iii dynamic fracture. Phys. Rev. Lett. 87, 045501 (2001)
- Khvoenkova, N., Delorme, M.: An optimal method to model transient flows in 3D discrete fracture network. In: IAMG Conference, vol. 2011, pp. 1238–1249 (2011)

- Kim, J., Tchelepi, H., Juanes, R.: Stability, accuracy, and efficiency of sequential methods for flow and geomechanics. SPE J. 16(2), 249–262 (2011)
- Kim, J., Tchelepi, H., Juanes, R.: Stability and convergence of sequential methods for coupled flow and geomechanics: fixedstress and fixed-strain splits. Comput. Methods Appl. Mech. Eng. 200(13-16), 1591–1606 (2011)
- Ladyzhenskaja, O., Solonnikov, V., Uralceva, N.: Linear and quasi-linear equations of parabolic type. Translations of mathematical monographs. AMS, vol. 23 (1968)
- 52. Laubach, S.E., Olson, J.E., Gale, J.F.: Are open fractures necessarily aligned with maximum horizontal stress? Earth Planet. Sci. Lett. **222**(1), 191–195 (2004)
- 53. Lee, S., Jensen, C., Lough, M., et al.: An efficient finite difference model for flow in a reservoir with multiple lengthscale fractures. In: SPE Annual Technical Conference and Exhibition. Society of Petroleum Engineers (1999)
- Lee, S., Lee, Y.J., Wheeler, M.F.: A locally conservative enriched galerkin approximation and efficient solver for elliptic and parabolic problems. SIAM J. Sci. Comput. 38(3), A1404–A1429 (2016)
- Lee, S., Mikelić, A., Wheeler, M., Wick, T.: Phase-field modeling of two phase fluid filled fractures in a poroelastic medium. Multiscale Modeling & Simulation 16(4), 1542–1580 (2018)
- Lee, S., Mikelić, A., Wheeler, M.F., Wick, T.: Phase-field modeling of proppant-filled fractures in a poroelastic medium. Comput. Methods Appl. Mech. Eng. 312, 509–541 (2016). Phase Field Approaches to Fracture
- Lee, S., Min, B., Wheeler, M.F.: Optimal design of hydraulic fracturing in porous media using the phase field fracture model coupled with genetic algorithm. Comput. Geosci. 22(3), 833–849 (2018)
- Lee, S., Reber, J.E., Hayman, N.W., Wheeler, M.F.: Investigation of wing crack formation with a combined phase-field and experimental approach. Geophys. Res. Lett. 43(15), 7946–7952 (2016)
- Lee, S., Wheeler, M.F.: Adaptive enriched galerkin methods for miscible displacement problems with entropy residual stabilization. J. Computational Phys. 331, 19 –37 (2017)
- Lee, S., Wheeler, M.F.: Enriched galerkin methods for two-phase flow in porous media with capillary pressure. J. Comput. Phys. 367, 65–86 (2018)
- Lee, S., Wheeler, M.F., Wick, T.: Iterative coupling of flow, geomechanics and adaptive phase-field fracture including blue level-set crack width approaches. Journal of Computational and Applied Mathematics (2016)
- Lee, S., Wheeler, M.F., Wick, T.: Pressure and fluid-driven fracture propagation in porous media using an adaptive finite element phase field model. Comput. Methods Appl. Mech. Eng. 305, 111–132 (2016)
- 63. Lee, S., Wheeler, M.F., Wick, T.: Srinivasan, S.: Initialization of phase-field fracture propagation in porous media using probability maps of fracture networks. Mech. Res. Commun. 80, 16–23 (2017). Multi-Physics of Solids at Fracture
- Mandal, T.K., Nguyen, V.P., Heidarpour, A.: Phase field and gradient enhanced damage models for quasi-brittle failure: a numerical comparative study. Eng. Fract. Mech. 207, 48–67 (2019)
- 65. Markert, B., Heider, Y.: Recent Trends in Computational Engineering - CE2014: Optimization, Uncertainty, Parallel Algorithms, Coupled and Complex Problems, chap. Coupled Multi-Field Continuum Methods for Porous Media Fracture, pp. 167–180. Springer International Publishing, Cham (2015)
- McClure, M.: An accurate and efficient method for calculating fluid exchange between fractures and matrix with a nonconforming mesh. arXiv:1709.02493 (2017)



- 67. Miehe, C., Hofacker, M., Schaenzel, L.M., Aldakheel, F.: Phase field modeling of fracture in multi-physics problems. Part ii. Coupled brittle-to-ductile failure criteria and crack propagation in thermo-elastic plastic solids. Comput. Methods Appl. Mech. Eng. 294, 486–522 (2015)
- Miehe, C., Mauthe, S.: Phase field modeling of fracture in multi-physics problems. part III. crack driving forces in hydroporo-elasticity and hydraulic fracturing of fluid-saturated porous media. Comput. Methods Appl. Mech. Eng. 304, 619–655 (2016)
- 69. Miehe, C., Mauthe, S., Teichtmeister, S.: Minimization principles for the coupled problem of darcy-biot-type fluid transport in porous media linked to phase field modeling of fracture. Journal of the Mechanics and Physics of Solids 82, 186–217 (2015)
- Miehe, C., Schaenzel, L.M., Ulmer, H.: Phase field modeling of fracture in multi-physics problems. Part i. Balance of crack surface and failure criteria for brittle crack propagation in thermo-elastic solids. Comput. Methods Appl. Mech. Eng. 294, 449–485 (2015)
- Miehe, C., Welschinger, F., Hofacker, M.: Thermodynamically consistent phase-field models of fracture: variational principles and multi-field fe implementations. International Journal of Numerical Methods in Engineering 83, 1273–1311 (2010)
- Mikelić, A., Wang, B., Wheeler, M.F.: Numerical convergence study of iterative coupling for coupled flow and geomechanics. Comput. Geosci. 18(3-4), 325–341 (2014)
- Mikelić, A., Wheeler, M.F.: Convergence of iterative coupling for coupled flow and geomechanics. Comput. Geosci. 17(3), 455–462 (2012)
- Mikelić, A., Wheeler, M.F., Wick, T.: A phase-field method for propagating fluid-filled fractures coupled to a surrounding porous medium. SIAM Multiscale Modeling and Simulation 13(1), 367–398 (2015)
- 75. Mikelić, A., Wheeler, M.F., Wick, T.: Phase-field modeling of a fluid-driven fracture in a poroelastic medium. Comput. Geosci. **19**(6), 1171–1195 (2015)
- Mikelić, A., Wheeler, M.F., Wick, T.: A quasi-static phase-field approach to pressurized fractures. Nonlinearity 28(5), 1371– 1399 (2015)
- Nguyen, T.T., Yvonnet, J., Zhu, Q.Z., Bornert, M., Chateau, C.: A phase-field method for computational modeling of interfacial damage interacting with crack propagation in realistic microstructures obtained by microtomography. Comput. Methods Appl. Mech. Eng. 312, 567–595 (2016)
- Noii, N., Wick, T.: A phase-field description for pressurized and non-isothermal propagating fractures. Comput. Methods Appl. Mech. Eng. 351, 860–890 (2019)
- Olson, J.E., Bahorich, B., Holder, J., et al.: Examining hydraulic fracture: Natural fracture interaction in hydrostone block experiments. In: SPE Hydraulic Fracturing Technology Conference. Society of Petroleum Engineers (2012)
- Perkins, T., Kern, L., et al.: Widths of hydraulic fractures. J. Petrol. Tech. 13(09), 937–949 (1961)
- Plahn, S.V., Nolte, K., Miska, S.: A quantitative investigation of the fracture Pump-Ln/flowback test. In: SPE Annual Technical Conference and Exhibition. Society of Petroleum Engineers (1995)
- Scovazzi, G., Wheeler, M.F., Mikelić, A., Lee, S.: Analytical and variational numerical methods for unstable miscible displacement flows in porous media. J. Comput. Phys. 335, 444–496 (2017)
- 83. Settari, A., Mourits, F.: A coupled reservoir and geomechanical simulation system. SPE J. **3**(3), 219–226 (1998)
- Settari, A., Walters, D.A.: Advances in coupled geomechanical and reservoir modeling with applications to reservoir compaction. SPE J. 6(3), 334–342 (2001)

- 85. Shiozawa, S., Lee, S., Wheeler, M.F.: The effect of stress boundary conditions on fluid-driven fracture propagation in porous media using a phase-field modeling approach. Int. J. Numer. Anal. Methods Geomech. 43(6), 1316–1340 (2019)
- Shovkun, I., Espinoza, D.N.: Fracture propagation in heterogeneous porous media: Pore-scale implications of mineral dissolution. Rock Mech. Rock. Eng.:1–15 (2019)
- Shovkun, I., Espinoza, D.N.: Propagation of toughnessdominated fluid-driven fractures in reactive porous media. International Journal of Rock Mechanics and Mining Sciences 118, 42–51 (2019)
- 88. Sun, S., Liu, J.: A locally conservative finite element method based on piecewise constant enrichment of the continuous galerkin method. SIAM J. Sci. Comput. **31**(4), 2528–2548 (2009)
- Tene, M., Bosma, S.B., Al Kobaisi, M.S., Hajibeygi, H.: Projection-based embedded discrete fracture model (pedfm). Adv. Water Resour. 105, 205–216 (2017)
- 90. U.S. Energy Information Administration: How much shale (tight) oil is produced in the united states? (2019). https://www.eia.gov/tools/faqs/faq.php?id=847&t=6
- Wang, W., Olson, J.E., Prodanović, M.: Natural and hydraulic fracture interaction study based on semi-circular bending experiments. In: Unconventional Resources Technology Conference, pp. 1645–1652. Society of Exploration Geophysicists, American Association of Petroleum . . . (2013)
- Wheeler, M.F., Srinivasan, S., Lee, S., Singh, M., et al.: Unconventional reservoir management modeling coupling diffusive zone/phase field fracture modeling and fracture probability maps. In: SPE Reservoir Simulation Conference. Society of Petroleum Engineers (2019)
- 93. Wheeler, M.F., Wick, T., Lee, S.: IPACS: Integrated phase-field advanced crack propagation simulator. An adaptive, parallel, physics-based-discretization phasefield framework for fracture propagation in porous media. Comput. Methods Appl. Mech. Eng. 367, 113124 (2020). Elsevier
- Wick, T.: Coupling fluid-structure interaction with phase-field fracture. J. Comput. Phys. 327, 67–96 (2016)
- 95. Wick, T., Lee, S., Wheeler, M.F.: 3D phase-field for pressurized fracture propagation in heterogeneous media. VI International Conference on Computational Methods for Coupled Problems in Science and Engineering 2015 Proceedings (2015)
- Witherspoon, P.A., Wang, J.S.Y., Iwai, K., Gale, J.E.: Validity of cubic law for fluid flow in a deformable rock fracture. Water Resour. Res. 16(6), 1016–1024 (1980)
- Wu, K., Olson, J.: Mechanics Analysis of Interaction between Hydraulic and Natural Fractures in Shale Reservoirs. In: Unconventional Resources Technology Conference, Denver, Colorado, 25-27 August 2014, pp. 1824–1841. Society of Exploration Geophysicists, American Association of Petroleum... (2014)
- Yoshioka, K., Parisio, F., Naumov, D., Lu, R., Kolditz, O., Nagel,
 T.: Comparative verification of discrete and smeared numerical approaches for the simulation of hydraulic fracturing. GEM International Journal on Geomathematics 10(1), 13 (2019)
- Zheltov, Y.P., Khristianovich, S.: On hydraulic fracturing of an oil-bearing stratum. Izv. Akad. Nauk SSSR. Otdel Tekhn. Nuk 5(3), 41 (1955)
- 100. Zhou, J., Huang, H., Deo, M., et al.: Simulation of hydraulic and natural fracture interaction using a coupled Dfn-Dem model. In: 50th US Rock Mechanics/Geomechanics Symposium. American Rock Mechanics Association (2016)
- Zimmerman, R.W., Bodvarsson, G.S.: Hydraulic conductivity of rock fractures. Transp. Porous Media 23(1), 1–30 (1996)

Publisher's note Springer Nature remains neutral with regard to jurisdictional claims in published maps and institutional affiliations.

